Nano Energy 74 (2020) 104815

Contents lists available at ScienceDirect

Nano Energy

journal homepage: http://www.elsevier.com/locate/nanoen

Surpassing lithium metal rechargeable batteries with self-supporting Li–Sn–Sb foil anode

Hui Xu [a,b,1], Sa Li [a,b,*,1], Xinlong Chen [a,b], Can Zhang [a,b], Zhuoqun Tang [a,b], Huimin Fan [a,b], Yue Yu [a,b], Wenjian Liu [a,b], Na Liang [a,b], Yunhui Huang [a,b,**], Ju Li [c,***]

[a] School of Materials Science and Engineering, Tongji University, Shanghai, 201804, China
[b] Institute of New Energy for Vehicles, Tongji University, Shanghai, 201804, China
[c] Department of Nuclear Science and Engineering and Department of Materials Science and Engineering, Massachusetts Institute of Technology, Cambridge, MA, 02139, USA

ARTICLE INFO

Keywords:
Lithium metal anode
Li–Sn–Sb alloy anode
Full cell
Volumetric energy density
Mesoscale science

ABSTRACT

Lithium metal rechargeable batteries (LMBs) degrade rapidly due to morphological instabilities as well as electrolyte consumption. As an alternative to Li_{BCC} metal foil, in this study, a self-supporting Li–Sb–Sn foil prepared by metallurgically alloying 5 wt%Sb-95 wt%Sn with Li_{BCC} is used as the anode in full-cell configurations. The electrochemical performance is highly competitive against equal-thickness pure Li_{BCC} foil, exhibiting much slower electrolyte degradation and less volume expansion: at the same amount of industrial-level electrolyte usage, $LiFePO_4$/Li–Sn–Sb(50 μm) full cells can sustain twice longer cycle life than $LiFePO_4$/Li_{BCC}(50 μm) cells. When pairing Li–Sn–Sb anode against high-areal-capacity $LiNi_{0.5}Co_{0.2}Mn_{0.3}O_2$(NCM523), $LiNi_{0.8}Co_{0.1}Mn_{0.1}O_2$(NCM811) and $LiCoO_2$(LCO) cathodes, the cell life is significantly improved compared to lithium metal batteries. In particular, a ~6 mAh cm^{-2} LCO/Li–Sb–Sn pouch cell delivers an initial energy density of 1027 Wh L^{-1}. Coulombic inefficiency analysis combined with morphological observations reveals that the excellent full-cell performance of Li–Sn–Sb is correlated with the smaller apparent volume expansion (thickening) and mesoscale features such as amount and type of porosity. Theoretical calculations and experimental measurements affirm doping 5 wt% Sb significantly suppresses porosity and long crack damage, evidenced by the smaller total porosity: 11% of Li–Sn–Sb versus 23% of Li–Sn, right after mechanical prelithiation, due to facile stress relief through the sliding grain boundaries (GBs), nano SnSb phase boundaries (PBs) and the buffering of soft residual Sn. The reaction kinetics and lithiation products of Sn electrode also change after doping Sb, breaking down a huge chemomechanical shock ($Sn \rightarrow Li_{22}Sn_5$) into several milder ones ($Sn \rightarrow Li_2Sn_5 \rightarrow LiSn \rightarrow Li_{22}Sn_5$) by nano features. While the Li-carrying ability of $Li_{22}Sn_5$ is similar to that of Li_{BCC}, the low volume expansion, cycling stability, better air stability and safety of Li–Sn–Sb foil mean it comprehensively surpasses Li_{BCC} metal foil anode.

1. Introduction

While rechargeable lithium metal batteries (LMBs) are regarded as the most promising candidates for next-generation high-density energy storage devices, their practical applications have been limited by poor cycle life and safety concerns [1]. After acquiring Moli Company and conducting in-depth research, NEC Corporation accepted the failure of LMBs commercialization because they could not overcome safety challenges caused by lithium metal morphological instabilities (LMI) [2,3]. Undeniably, lithium metal has great merits because of its high theoretical capacity (3860 mAh g^{-1} and 2062 mAh cm^{-3}) and low electrochemical potential (e.g. -3.04 V vs. the standard hydrogen electrode, SHE) [4]. But as a hostless anode, the plating/stripping of Li_{BCC} in body-centered cubic (BCC) crystal structure, is accompanied by dendrite

* Corresponding author. School of Materials Science and Engineering, Tongji University, Shanghai, 201804, China.
** Corresponding author. School of Materials Science and Engineering, Tongji University, Shanghai, 201804, China.
*** Corresponding author.
E-mail addresses: lisa@tongji.edu.cn (S. Li), huangyh@tongji.edu.cn (Y. Huang), liju@mit.edu (J. Li).
[1] These authors contributed equally to this work.

https://doi.org/10.1016/j.nanoen.2020.104815
Received 7 January 2020; Received in revised form 6 April 2020; Accepted 7 April 2020
Available online 23 April 2020
2211-2855/Published by Elsevier Ltd.

growth, electrode pulverization [5], electrolyte consumption and apparent volume expansion [6]. When Li_{BCC} dendrites penetrate through separator, short-circuiting happens, leading to fire or explosion, seriously threatening personal and property safety. The poor cycle life of LMBs is another essential problem [7]. Serious surface area proliferation due to LMI drives side reactions with the electrolyte, which irreversibly consumes electrolyte and lithium inventory, disrupts electronic percolation and causes huge apparent expansion of the electrode thickness [8]. Thus, the cycle life of LMBs depends sensitively on the amount and type of electrolyte used, as well as excess lithium inventory (the amount of cyclable lithium beyond that carried by the cathode). Although a fresh Li_{BCC} metal foil starts out fully dense, the non-active volume fraction ϕ ($\phi \equiv 1-\rho/\rho_{ideal}$) of the foil electrode will increase after cycling, that includes volume taken by electrolyte decomposition products (e.g. SEI), parasitic voids and inactive lithium fragments [9], seriously lowering the actual volumetric energy density. In order to overcome these problems of pure lithium metal, extensive efforts have been focused on solid electrolyte development for avoiding short circuits [10–13], interface treatment and electrolyte optimization for better lithium deposition [14–16] as well as 3D electrode structure fabrication for constraining volume expansion [17,18], and so on.

Developing self-supporting Li-M (M = C, Si, Sn, Al, etc.) alloy foil to substitute Li_{BCC} foil anode is another approach. Due to the high packing density/concentration of lithium (PD_{Li}) [19] of $Li_{22}Sn_5$ (materialsproject.org mp-1198729) PD_{Li} = 22/479.68 Å^3 = 1/21.8 Å^3, compared to Li_{BCC} (mp-135): PD_{Li} = 1/20.121 Å^3, prelithiated Sn foil (Li–Sn) is a very potent Li carrier volumetrically [20]. This should eliminate Li_{BCC} precipitation even at large rates due to higher equilibrium electrochemical potential (e.g. Sn at ~0.4 V vs. Li/Li$^+$) [21,22]. For example, Cui et al. [23] have reported the stable lithium plating/stripping of their freestanding Li_xM/graphene electrode (M = Si, Sn, and Al), prepared by firstly heating the mixture of M nanoparticles and Li_{BCC} under inert atmosphere for Li_xM preparation and then casting/filtrating the suspension of Li_xM and graphene for shaping. Considering metallic tin and aluminum foils have intrinsically superior electronic conductivity and compressed density [24,25], in our previous work, we developed an easy-to-implement, roll-to-roll mechanical prelithiation (MP) method to produce Li–Sn and Li–Al foils at room temperature [26]. The as-prepared self-supporting Li–Sn and Li–Al electrodes not only show striking air stability but also achieve an ultrahigh initial Coulombic efficiency (ICE) of ~90%–94% and long full-cell cycle life, e.g. $LiFePO_4$/Li–Sn and $LiFePO_4$/Li–Al with a commercial-scale areal capacity of ~2.65 mAh cm^{-2} achieved 200 cycles and 100 cycles in full-cell cycling, respectively. While prelithiated alloy foil anode has evident advantages, e.g. Li_{BCC} dendrite-free and safety enhancements [27–29], they still face severe challenges for practical applications including large volume change, excessive SEI formation and poor cycle life, etc. [30]. Previously, Li–Sn alloy showed significant apparent electrode thickening with cycling, for instance, a Li–Sn foil of 100 μm thickness thickened to 351 μm after full-cell cycling of 200 cycles, which seriously degrades the actual volumetric capacity. In addition to the absolute volume expansion caused by lithiation reactions, such apparent thickening of Sn foil also originates from the cracks, parasitic voids formation (see Fig. S1) and electrolyte decomposition products accumulation (see Fig. S2). In previous work, we reduced cracking and suppressed electrode thickening to a certain extent by grain size refinement, where the grain boundaries (GBs) in foil electrode was shown to be effective sliding systems to relieve stress and avoid large cracks. However, such improvement is still limited because Sn foil is easy to experience re-crystallization and grain growth at the room temperature, as it is already at 2/3 of the absolute melting temperature of Sn (T/T_M = 0.66) [31], so the starting grain size is still quite coarse, and GB density is not as high as desired.

Finely dispersed second-phase precipitates not only pin down grain growth to refine the initial grain size $D_{initial}$ [32–34], but they can also be electrochemically active [35]. For example, after doping Sb to Sn matrix to obtain SnSb intermetallic precipitates, they will undergo the following reactions upon electrochemical lithiation or mechanical prelithiation (MP),

$$\text{During the first step: } SnSb + 3Li \rightarrow Li_3Sb + Sn \text{ (at ~0.8 V)}, \quad (1)$$

$$\text{2nd step: } Sn + xLi \rightarrow Li_xSn \ (0 < x \leq 4.4, \text{ at 0.7–0.4 V}). \quad (2)$$

So on one hand, the starting SnSb precipitates can refine Sn grain and increase the density of GBs and phase boundaries (PBs) [36,37], and on the other hand, the lithiation of SnSb produces nano Sn/Li_xSn/Li_3Sb particles that contribute extra PBs [38]. Thus, doping Sb in Sn matrix may have double effects for stress relief. When stress is released significantly by enough sliding GBs and PBs [39,40], the number and size of cracks will be reduced, and the apparent thickening caused by porosity and accumulated SEI will be subsequently reduced. The occurrence of dead particles caused by the loss of electronic percolation (surrounded on all sides by electronically insulating SEI or liquid electrolyte) will be reduced in cycling as well, because as long as one of the metal/metal GB/PBs surrounding an active grain or grain cluster remains, it can maintain electronic percolation to the outside and cycling activity. Here we can draw an analogy between foil anode and the traditional slurry coating anode. If we consider an active metallic grain in foil to be equivalent with an active particle in slurry, then the GB/PBs play the dual role of conductive agent and binder, as metal/metal GB/PB conducts electrons across to the active particle and simultaneously can transmit tensile stress, where a sliding GB/PB is akin to a more stretchable binder [41]. It is well known that conductive agents and binders play a huge role for the slurry electrodes, especially for high volume expansion anode materials like Si [42], thus it should not be surprising that the type and concentration of GB/PBs impact the cycling stability and apparent volume expansion of the metallic foil electrode, as they are effectively "deformable conductive binders" (since GBs can slide and migrate), and the smaller the grain size, the higher the volumetric concentration of such "conductive binders" which is proportional to 1/D, where D is the grain size. In this paper, we employed 5 wt% Sb-95 wt%Sn foil (SnSb/Sn) as a starting material and prepared self-supporting Li–Sn–Sb foil electrode by mechanically rolling 5 wt% Sb-95 wt%Sn and Li_{BCC} foils together, to induce mechanical prelithiation (MP), a solid-state metallurgical reaction that is accomplished at room temperature under ~30 MPa pressure [26,43]. The as-formed Li–Sn–Sb foil electrode exhibited quantitatively superior electrochemical performance than Li_{BCC} foil in multiple ways, including excellent full-cell cycle performance, no risk of lithium dendrites, as well as better air stability and much lower fire and short-circuiting risk.

2. Experimental procedures

5 wt%Sb-95 wt%Sn foil (50–150 μm thick, Zhenjiang Fan Yada Electronic Technology Co., Ltd.) was punched into a disc with a diameter of 12 mm and then directly used as working electrode. The mechanical prelithiation was carried out as following: pressing two 5 wt% Sb-95 wt%Sn foils sandwiching a Li_{BCC} foil (China Energy Lithium Co., Ltd.) in the middle with a roller (MSK-2150, Shenzhen Kejing Star Technology, LTD.). The as-prepared prelithiated foil was punched into disc or designed dimensions of pouch cell and then directly used as anode electrode. The commercial $LiFePO_4$ and NCM523 cathodes were purchased from MTI. NCM811 and LCO cathodes were homemade.

Grain and phase microstructures of 5 wt%Sb-95 wt%Sn foil were observed *via* optical microscopy (6XB-PC, Shanghai optical instrument factory) and transmission electron microscopy (TEM, FEI Tecnai TF20, JOEL 2100F). The solution consisting of 1.5 vol.% HCl, 1 vol.% HNO_3 and 97.5 vol.% methanol was employed to corrode foil for grain observation. The surface and cross-section morphologies were observed *via* a field emission scanning electron microscope (SEM, FEI Quanta 200). The phase structure of foil was identified by X-ray diffraction (XRD, Bruker AXS GMBH GERM D8) with CuK_α radiation (λ = 1.54184

Å). The signal of diffraction angles (2θ) between 10° and 80° was collected at a scan rate of 3° min^{-1}, Kapton tape was used to protect the lithiated foils from air corrosion.

CR2025 coin-cell tests were performed on Neware CT-4008. The applied separator was Celgard 2400. The electrolyte of $LiFePO_4$/Li–Sb–Sn full cell was 1 M $LiPF_6$ solvated in EC/DEC (v/v = 1:1) with 10% FEC and 1% VC as additives, the electrolyte of NCM523/Li–Sb–Sn, NCM811/Li–Sb–Sn and LCO/Li–Sb–Sn full cells was purchased from Hubei Jiubang New Energy Technology Co., Ltd. (NP6054A1). The CV measurements of 5 wt%Sb-95 wt%Sn/Li_{BCC} and Sn/Li_{BCC} cells were performed on an electrochemical work station (CHI660E, Shanghai Chen Hua Instrument Co., Ltd.), scanning from 1.5 V to 0 V at a rate of 0.1 mV s^{-1}. $LiFePO_4$/Li–Sb–Sn cells were charged to 3.8 V and then discharged to 2 V at 0.3C. NCM523/Li–Sb–Sn and NCM811/Li–Sb–Sn full cells were charged to 4.2 V and then discharged to 2.6 V at 0.3 C. LCO/Li–Sb–Sn were charged to 4.1 V and then discharged to 2.6 V at 0.3 C. The puncture experiments were carried out in Tianmu Lake Institute of Advanced Energy Storage Technologies.

3. Results and discussion

Thermodynamically, SnSb intermetallic has higher equilibrium potential than Sn matrix, and thus will be lithiated first [32], influencing the later kinetics. Thus, the distribution and size of intermediate phase SnSb particles in 5 wt%Sb-95 wt%Sn were characterized by optical microscopy, SEM and TEM. As shown in Fig. S3, the little black dots circled by the red dash line at grain (Sn) boundaries are SnSb particles. SEM also showed considerable protruding nano particles in the foil matrix (Fig. 1a) and EDS elemental analysis proved that these nano particles were the SnSb intermetallic phase (Fig. S4). Note that due to the imprecision of EDS, the determined atom ratio of Sn and Sb elements is not strictly following the ratio of 1:1, e.g. Sn is 50.83% and Sb is 37.35%. TEM revealed a ~500 nm wide SnSb particle imbedded into Sn matrix (Fig. 1b). Afterwards, we prepared the free-standing Li–Sb–Sn electrode by mechanical prelithiation. The specific preparation processes (see Fig. S5) and operating parameters were identical with our previously reported method [26,43]. After the room-temperature solid-state reactions (1), (2), we allow metallurgical reaction

$$5Sn_{HCP} + 22Li_{BCC} \rightarrow Li_{22}Sn_5 \text{ (at 0.4 V vs. Li/Li}^+\text{)} \quad (3)$$

of the matrix to finish under pressure. Note that Sn_{HCP} of (3) indicates tin phase with hexagonal close-packed structure. After sandwiching a Li_{BCC} foil between two 5 wt%Sb-95 wt%Sn foils and pressing (see Fig. S5a), lithium will be fully 'absorbed' into the Sn-based foils (see Fig. S5b). The product could be easily separated into two pieces of identical free-standing Li–Sb–Sn foils, by mechanical peeling (see Fig. S5c). Thus, such prelithiation method is easy to achieve large-scale preparation of foil electrode. As shown in Fig. 1c, where two 10 cm × 2.8 cm × 50 μm lithiated foils are obtained by rolling two 7.5 cm × 2.6 cm × 50 μm 5 wt%Sb-95 wt%Sn foils sandwiching one 7.5 cm × 2.6 cm × 50 μm Li_{BCC} foil in the middle. After mechanical prelithiation, an obvious lateral area expansion of ~44% has occurred (Fig. S6 and Table S1) because the externally applied rolling pressure during MP and the heat released made Li and Sn foils experience plastic deformation. According to XRD analysis (PDF#-18-0753), the characteristic peaks belong to $Li_{22}Sn_5$ (see Fig. 1d), with no obvious signals of Li_3Sb or other Li–Sn intermetallics. Besides, according to SEM, as shown in Fig. 1e, the 50 μm thick Li–Sb–Sn

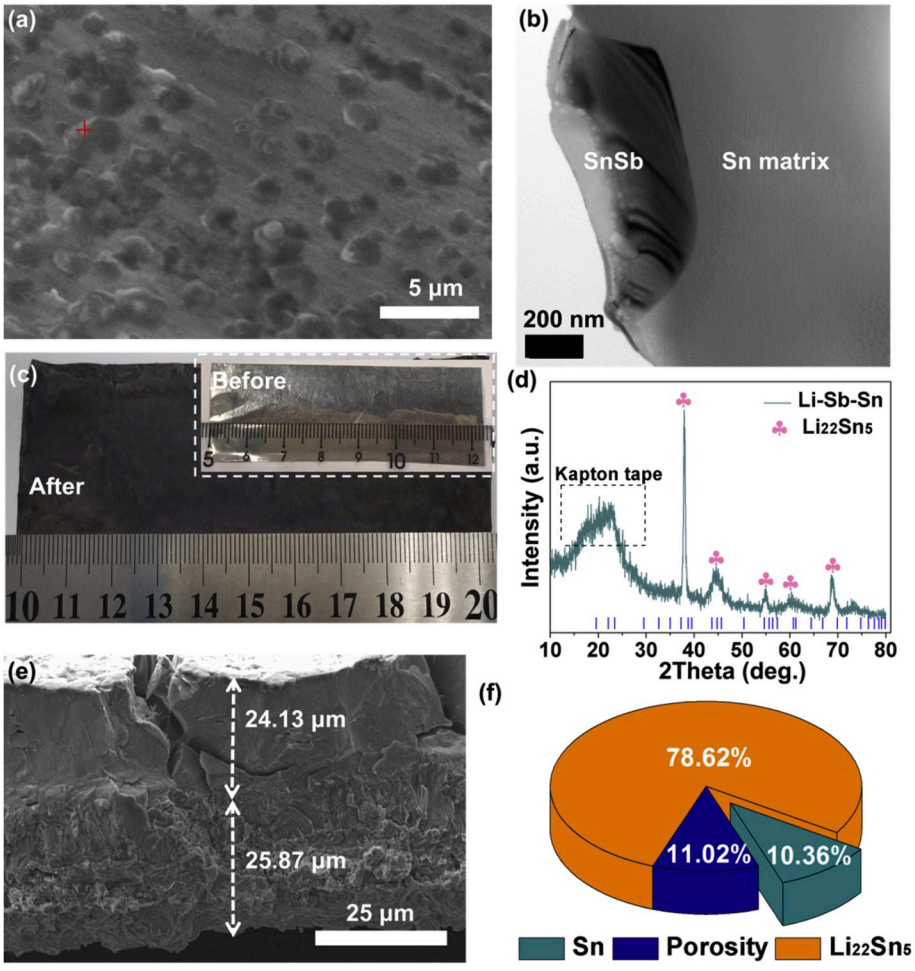

Fig. 1. Characterizing 5 wt%Sb-95 wt%Sn foil and Li–Sb–Sn electrode prepared by mechanical prelithiation. a) SEM image of 5 wt%Sb-95 wt%Sn foil. Some protruding nano particles were observed in the matrix. b) TEM image of intermediate phase SnSb particle embedded in Sn matrix. c) Digital photo of Li–Sb–Sn prepared by mechanically pressing two 7.5 cm × 2.6 cm × 50 μm 5 wt%Sb-95 wt%Sn foils sandwiching one 7.5 cm × 2.6 cm × 50 μm Li foil in the middle. d) XRD result of Li–Sb–Sn. Only $Li_{22}Sn_5$ phase was determined. e) SEM image of Li–Sb–Sn electrode. The electrode consists of two layers, including 24.1 μm thick porous reacted part and 25.9 μm thick unreacted 5 wt%Sb-95 wt%Sn part. f) Percentages of porosity (the blue), retained Sn (the green) and $Li_{22}Sn_5$ (the orange) in the reacted layer of Li–Sb–Sn.

consists of a 24.1 μm thick reacted layer with porosity, and a 25.9 μm thick unreacted 5 wt%Sb-95 wt%Sn that is still fully dense. The reacted layer (Fig. 1e, the top layer) consisted of lithiation products, cracks (porosity), as well as unreacted residual soft Sn ("retained Sn", akin to the "retained austenite" phase in martensitic steels which improves the ductility). We calculated the individual percentage of three components in the Li–Sb–Sn reacted layer, in Supplementary Note 1 based on the theoretical volumes of Sn_{HCP}, Li_{BCC} and $Li_{22}Sn_5$ phases, and show the result in Fig. 1f.

As a quantitative measure of the chemomechanical shock damage from the mechanical prelithiation [41], the porosity of the reacted layer in Li–Sb–Sn foil was estimated to be 11.05%, which is much lower than that of Li–Sn (23%, see Supplementary Note 2) prepared in an identical manner. The larger porosity of Li–Sn not only indicates the more serious damage but also directly leads to the electrical conductivity deterioration. Our previous works had revealed the metal/metal GB/PB can effectively relieve stress and maintain conductivity, like the stretchable binder and conductive agent of tradition electrode. For example, silver, copper-doped Sn foil [43] or Mn, Si-doped Al foil [44] with more abundant GB/PBs has less damage and better electrical conductivity. But for Li–Sn, as shown in Fig. S7a, deep cracks are widely distributed in the Li–Sn electrode from top to bottom, which break the originally dense foil into pieces. Even on each piece of shard (marked with yellow in Fig. S7a), secondary damage also can be found (marked with yellow in Fig. S7b). These cracks destroy electronic path connectivity by splitting originally adjacent conductive grain/grain clusters that allow electrons to hop across like in conductive agents. However, compared to the severely damaged Li–Sn, Li–Sb–Sn has less damage (see Fig. S7c) and almost no secondary cracks on the shard (see Fig. S7d). These mesoscale features right after mechanical prelithiation strongly influence the subsequent electrochemical cycling stability.

The account in Supplementary Note 1 showed that the Li-absorbing ability of Sn based foil is quite extraordinary, for example, just 7.85 μm 5 wt%Sb-95 wt%Sn (50 μm/1.44–25.87 μm) absorbed 17.36 μm of Li_{BCC} (50 μm/2/1.44) (thickness divided by 1.44 considering lateral area expansion of ~44%), and grew to an apparent thickness of 24.13 μm including the 11.05% porosity. Furthermore, as shown in Fig. S8, the electrochemically retrievable lithium inventory of Li–Sb–Sn is ~3.12 mAh cm^{-2}, equivalent to 15.6 μm thick of Li_{BCC} which is nearly equal to the calculation value 17.36 μm, affirming the validity of our calculation. We speculate the small deviation is because the calculation did not take into account the Li_3Sb formations, as well as volume expansion making some lithiation products inactive. The gravimetric capacity of Li–Sb–Sn electrode is shown in Fig. S9a and S9b: the specific lithiation capacity of Li–Sb–Sn is ~563.92 mAh g^{-1} and delithiation capacity is ~748.29 mAh g^{-1}. Such potent lithium absorbing and desorbing ability is the basis that lithiated Sn foil can be competitive against Li_{BCC} foil.

To compare the full-cell cycling performance of our self-standing Li–Sb–Sn with equal thickness pure Li_{BCC} electrode, here, we adopted the standard ester electrolyte (1 M $LiPF_6$ in EC/DEC (v/v = 1:1) with 10% FEC, 1% VC) and explored the influence of electrolyte weight on cycle life of $LiFePO_4$/Li–Sb–Sn full cell and $LiFePO_4/Li_{BCC}$ with an areal capacity of ~2.65 mAh cm^{-2}. For reference, the industrially standard usage of this kind of electrolyte for $LiFePO_4$/graphite cell is 6–8 g (electrolyte) Ah^{-1}. As shown in Fig. 2a, when the electrolyte used was 20 μL for the cathode areal capacity of 2.65 mAh cm^{-2} in CR2025 coin-

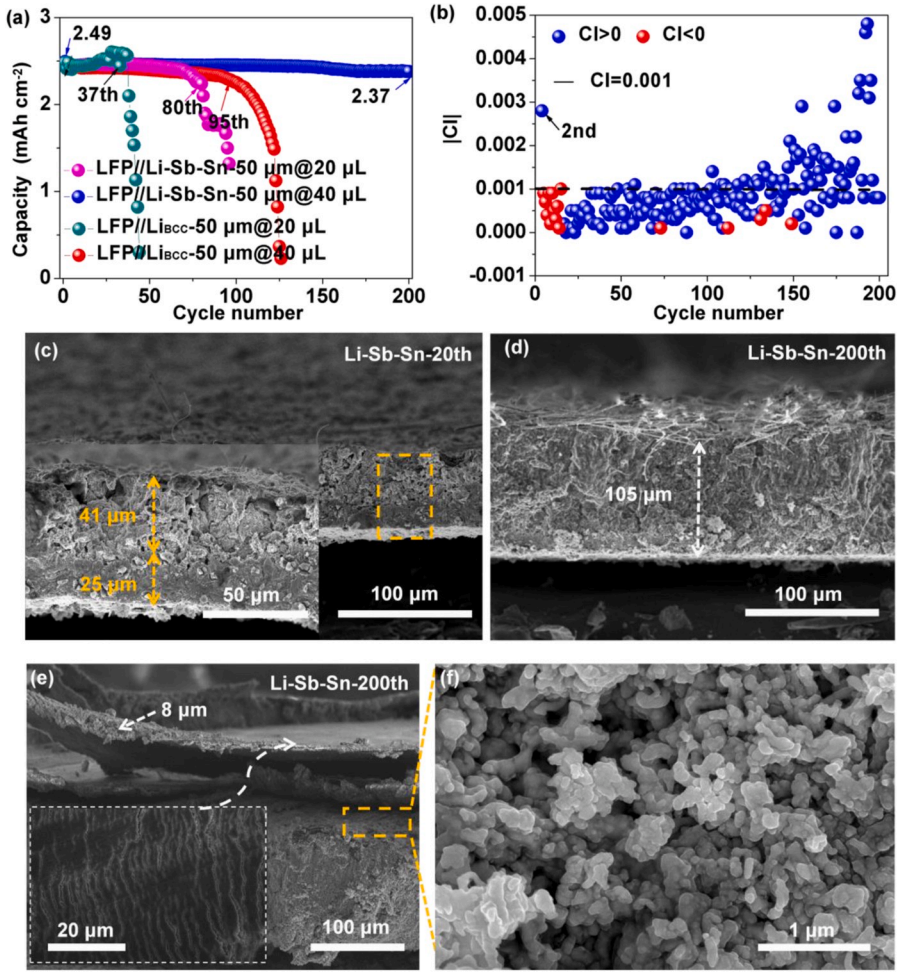

Fig. 2. Influence of electrolyte amount on cycle performance of $LiFePO_4$/Li–Sb–Sn full cell and Li–Sb–Sn electrode thickening analysis after full-cell cycling. a) Cycle performance of $LiFePO_4$/Li–Sb–Sn full cell and $LiFePO_4/Li_{BCC}$ cell respectively with electrolyte of 20 μL (e.g. 7.56 g Ah^{-1}) and 40 μL (e.g. 15.12 g Ah^{-1}). b) Columbic inefficiency (CI≡100%-Columbic efficiency (CE)) analysis of $LiFePO_4$/Li–Sb–Sn full cell with 40 μL electrolyte. The blue dot is CI > 0 and the red is CI < 0. The black dotted line is |CI| = 0.001. c) SEM image of Li–Sb–Sn electrode after full-cell cycling of 20 cycles. d, e) SEM images of Li–Sb–Sn after full-cell cycling of 200 cycles. f) SEM image of Li–Sb–Sn matrix after peeling off the top dense protective layer. There are lots of ~200 nm sized Sn particles.

cell (e.g. 7.56 g Ah^{-1}), $LiFePO_4/Li_{BCC}$ cell failed rapidly after just 37 deep charge/discharge cycles (Fig. 2a, the olive), due to electrolyte contamination and drying out (see Fig. S10), with the cell failing to reach the cutoff voltage 3.8 V (Fig. S11) and a precipitously dropping CE at 28th cycle (Fig. S12). In contrast, $LiFePO_4$/Li–Sb–Sn full cell (Fig. 2a, the magenta) stably charged and discharged 80 cycles, indicating the side reactions between electrolyte and Li–Sb–Sn were less severe. We further increased electrolyte to 40 μL (e.g. 15.12 g Ah^{-1}) to examine long-term cycling of Li–Sb–Sn electrode. As shown in Fig. 2a (the blue), after 200 cycles, $LiFePO_4$/Li–Sb–Sn stably kept at ~2.37 mAh cm^{-2} and achieved a capacity retention of 95.2%. In contrast, $LiFePO_4/Li_{BCC}$ (Fig. 2a, the red) remained stable for 95 cycles and then rapidly failed. We analyzed the Coulombic inefficiency (CI≡100%-Columbic efficiency) [45] of $LiFePO_4$/Li–Sb–Sn full cell with 40 μL electrolyte and found nearly 80% of CIs of 200 cycles were less than 0.001 (see Fig. 2b), meaning the corresponding CE was up to 99.9%. It should be noted that in this paper, adopting CI instead of CE is because CI can more sensitively correlate with major structural repairs of SEI and irreversible SEI growth per cycle [45].

SEM observations suggested that the excellent full-cell performance and favorable CE of Li–Sb–Sn electrode originated from its significantly less nominal volume expansion. As shown in Fig. 2c, Li–Sb–Sn electrode thickened to 66 μm after full-cell cycling of 20 cycles, including 41 μm thick reacted layer and 25 μm thick intact layer that was not yet involved in electrochemical reactions (Fig. 2c, the inset). The electrode became homogeneously dense and sturdy after 200 cycles (see Fig. 2d). Even though the electrode had thickened to 105 μm eventually from the initial 50 μm, this was still far more acceptable than Li_{BCC}. As shown in Fig. S13, the 50 μm Li_{BCC} foil pulverized and totally lost mechanical strength after 120 cycles. With further analysis, we found the Li–Sb–Sn electrode surface was covered by a layer of ~8 μm thick film that was capable of being bent and wound (Fig. 2e and Fig. S14), which seemed to prevent the continuous electrolyte corrosion. After peeling off this ~8 μm layer, lots of ~200 nm sized Sn particles could be observed (Fig. 2f). So the top film acted as a solid electrolyte barrier that effectively blocked liquid electrolyte penetration and suppressed continuous SEI formation during the future cycling. Conversely, we believe that such a sturdy protective layer could form and maintain because the matrix experienced less geometry change, for reason to be shown next.

Cyclic voltammetry (CV) shows doping Sb evidently changed the electrochemical kinetics and lithiation products of Sn foil. As shown in Fig. S15, except for Li_3Sb peak at ~0.82 V, 5 wt%Sb-95 wt%Sn/Li_{BCC} cell also had another three lithiation peaks at ~0.67 V (for Li_2Sn_5), ~0.51 V (for LiSn) and ~0.34 V (for $Li_{22}Sn_5$), respectively; but pure Sn/Li_{BCC} cell only had a single $Li_{22}Sn_5$ peak at ~0.3 V [46]. Thus, after doping Sb, the originally fierce volume change of pure Sn foil electrode could be catalyzed into several milder ones, which greatly eased the mechanical stress in each step. We speculate that the formation of "lithium-poor" Li_2Sn_5 and LiSn phases in 5 wt%Sb-95 wt%Sn/Li_{BCC} may be attributed to the nano Sn particles created from (1), which is kinetically more favorable to engender the "lithium-poor" Li_2Sn_5 and LiSn products later because of smaller particle size. In previous work, we had revealed the lithium diffusion mainly takes place along grain boundaries at the beginning of lithiation [41,43,44]. Therefore, for a pure Sn foil having large grain sizes, the initial reaction paths are scarce, resulting in highly inhomogeneous lithium flux, geometric incompatibility and stress, mainly gathering around GBs initially. In addition, Li diffusion is faster in lithium-rich phase (e.g. 5.9×10^{-7} cm^{-2} s^{-1} for $Li_{22}Sn_5$ but 8×10^{-8} cm^{-2} s^{-1} for LiSn at 25 °C) [19], so for a pure Sn foil with large grain size and lots of interior grounds to cover, it is more kinetically favorable to form a single lithium-rich phase $Li_{22}Sn_5$. But for 5 wt% Sb-95 wt%Sn with smaller grain size and nano Sn particles on GBs from (1), the reaction kinetics is branched. When galvanostatically lithiating foils to 10 mAh cm^{-2} at 0.1 C, unlike Sn/Li_{BCC} cell that dropped to ~0.4 V directly and only formed $Li_{22}Sn_5$ (Fig. S16, the red) which entails a huge volume change, 5 wt%Sb-95 wt%Sn/Li_{BCC} cell had an evident long inclined lithiation plateau at ~0.7–0.6 V, which corresponds to the generation of lithium-poor Li_2Sn_5 and LiSn phases, contributing a capacity of ~4 mAh cm^{-2} (Fig. S16, the blue). Therefore, the effects of doping Sb are significant, and helpful in reducing the stress shock and suppressing volume expansion because it goes through the "lithium-poor" phases Sn→Li_2Sn_5→LiSn→$Li_{22}Sn_5$, instead of a "direct flight" to the lithium-rich phase Sn→$Li_{22}Sn_5$ that is a huge chemomechanical shock and more likely to damage the foil integrity. As shown in Fig. S17, Li–Sn foil reacted deeply from the top to bottom and became loose, porous after only 100 cycles. Thus, Li–Sn thickened by ~86 μm from initial 46.05 μm to 132 μm. However, even after performing 200 cycles (see Fig. 2f), Li–Sb–Sn had a denser structure due to a series of intermediate phase transformations.

Although the superior $LiFePO_4$/Li–Sb–Sn full-cell performance strengthens the application prospect of such free-standing electrode (as compared to the graphite slurry electrode, Li–Sb–Sn does not require the heavy and expensive Cu current collector as backing), the low voltage and low areal capacity of $LiFePO_4$ cathode still limit capacity output of the full cell. As shown in Fig. S18, in a ~3 mAh LFP/Li–Sb–Sn full cell, the *utilized* gravimetric capacity of Li–Sb–Sn is only ~171.23 mAh g^{-1} (=3 mAh/(17.52×10^{-3} g)), far below its theoretical capacity – in other words the state of charge (SOC) of the anode is still low - due to insufficient areal capacity of the matching cathode.

To this end, Li–Sb–Sn was further paired against NCM523, NMC811 and LCO cathodes respectively for full cells. As shown in Fig. 3a (the red) and Fig. S19, NCM523/Li_{BCC} cell with areal capacity of ~3 mAh cm^{-2} and electrolyte amount of 40 μL (14.81 g Ah^{-1}) showed faster capacity decay and its capacity retention dropped below 80% after only 45 cycles at 0.2 C, but NCM523/Li–Sb–Sn performed stably for 150 cycles, and achieved a capacity retention of 89.53% at the same rate (Fig. 3a, the blue, and Fig. S20). This highlights the significant superiority of the Li–Sb–Sn foil electrode versus the Li_{BCC} foil electrode in high-energy-density batteries.

We also found the CI of NCM523/Li_{BCC} drastically increased to ~0.25 after 45th cycle (Fig. 3b, the orange) but that of NCM523/Li–Sb–Sn still kept at ~0.01 (see Fig. 3b, the olive), which indicated Li–Sb–Sn actually experienced fewer side reactions with electrolyte due to the more stable electrode. Furthermore, unlike NMC811/Li_{BCC} cell which showed linear attenuation in capacity and lasted only for 56 cycles (Fig. 3c, the red), NMC811/Li–Sb–Sn cell with areal capacity of ~4 mAh cm^{-2} and electrolyte amount of 60 μL (13.33 g Ah^{-1}) achieved 85.4% capacity retention after 100 cycles (Fig. 3c, the blue). Clearly, pairing Li–Sb–Sn electrode against NCM cathodes can achieve better full-cell performance, so we believe more attention should be paid to such free-standing Li–Sn based foil electrodes instead of focusing on lithium metal foil only.

Considering that LCO cathode has the highest compaction density (e.g. ~5 g cm^{-3}), pairing LCO against Li–Sb–Sn anode can achieve an ultra-high volumetric energy density for the full cell. Thus, firstly, a LCO/Li–Sb–Sn coin cell with areal capacity of ~6 mAh cm^{-2} was fabricated and the electrolyte amount was 70 μL (11.67 g Ah^{-1}). As shown in Fig. 3d (the blue) and Fig. 3e, the remaining capacity of LCO/Li–Sb–Sn was 5.28 mAh cm^{-2} and the capacity retention was ~90% after 50 cycles but LCO/Li_{BCC} showed obvious decay after 35th cycle (Fig. 3d, the red). And its capacity dropped to ~4.21 mAh cm^{-2} after 50 cycles, the capacity retention was only ~72%. The rapid decay of LCO/Li_{BCC} is attributed to Li_{BCC} foil pulverization and electrolyte depletion with deep cycling. Besides, due to pairing against the high-areal-capacity LCO cathode, the utilized specific capacity of Li–Sb–Sn can be increased to 337.98 mAh g^{-1} (see Fig. S21), significantly increasing the state of charge (SOC) of the anode. To further highlight the volumetric energy performance, we have assembled a 2.5 cm × 2.8 cm sized LCO/Li–Sb–Sn pouch cell (see Fig. 3f, the inset) and its cycle capacity and energy were plotted in Fig. S22 and Fig. S23. Encouragingly, although the Li–Sb–Sn electrode thickened to 75 μm after 1st cycle from 50 μm, its volumetric energy was still 1027 Wh L^{-1}. After 20 cycles, even though the thickness

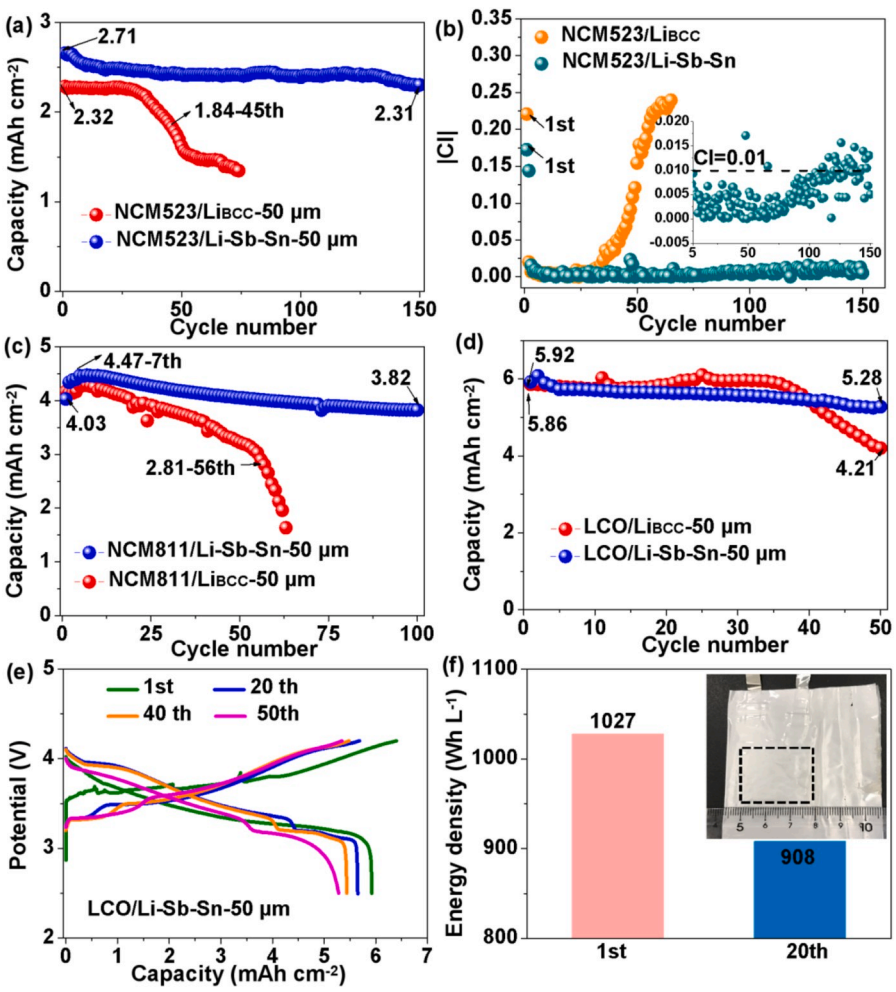

Fig. 3. Full cells pairing Li–Sb–Sn againstNCM523, NCM811 and LCO cathodes, respectively, for higher voltage and areal capacity. a) Cycle performance of NCM523/Li–Sb–Sn (the blue) and NCM523/Li_{BCC} (the red). b) Columbic inefficiency (CI) analysis of NCM523/Li–Sb–Sn (the olive) and NCM523/Li_{BCC} (the orange). c) Cycle performance of NCM811/Li–Sb–Sn (the blue) and NCM811/Li_{BCC} (the red). d) Cycle performance of LCO/Li–Sb–Sn (the blue) full cell and LCO/Li_{BCC} cell (the red). e) Potential-Capacity profiles of LCO/Li–Sb–Sn full cell. f) Volumetric energy density of LCO/Li–Sb–Sn pouch cell. And the inset is the digital photo of pouch cell (2.5 cm × 2.8 cm).

increased to 93 μm, the volumetric energy still reached 908 Wh L^{-1} (see Fig. 3f and Table S3), which is significantly superior to the commercial Li-ion batteries with 750 Wh L^{-1} discharge energy. This means Li–Sb–Sn electrode is much closer to applications. In future work, we believe the performance of Li–Sb–Sn can be further improved by carefully designs, i.e. building artificial SEI [47–49]. For example, we have roughly designed a PEO artificial SEI on Li–Sb–Sn surface. As shown in Fig. S24, Li–Sb–Sn@PEO achieved less thickening and denser structure than the naked Li–Sb–Sn.

In addition to full-cell electrochemical performance, we have also studied the safety of Li–Sb–Sn foil, including the risk of short circuiting at deep plating/stripping, air stability as well as fire safety. Firstly, as we mentioned, depositing and stripping Li_{BCC} near 0 V is precarious especially at large current density and large areal capacity due to lithium metal morphological instabilities (LMI) such as dendrites [5]. However, Li–Sb–Sn as an alloy electrode has higher lithiation potential (e.g. 0.4–0.8 V vs. Li/Li^+) than Li_{BCC} precipitation potential, which removes the Li_{BCC} dendrites risk for Li–Sb–Sn. As shown in Fig. 4a, Li–Sb–Sn/-Li–Sb–Sn symmetrical cell fabricated by 200 μm thick Li–Sb–Sn electrodes could stably plate/strip lithium for more than 120 h at 10 mAh cm^{-2} and 10 mA cm^{-2}, but Li_{BCC}/Li_{BCC} symmetrical cell with pure Li_{BCC} metal foils of the same thickness suffered a rapid short circuit just after 20 h (Fig. 4a, the red). Note that in order to obtain sufficient and homogeneously distributed lithium inventory, here, 200 μm thick Li–Sb–Sn was prepared by rolling one 180 μm Li_{BCC} foil on one 120 μm 5 wt%Sb-95 wt%Sn foil, with similar amount of area expansion as before (180 μm/1.44 = 125 μm of Li_{BCC} reacting with 120 μm/1.44 = 83 μm 5 wt%Sb-95 wt%Sn foil). The electrochemically retrievable lithium inventory was a gigantic value of ~22 mAh cm^{-2} (see Fig. S25). Eventually, despite the Li–Sb–Sn/Li–Sb–Sn cell died from large polarization (note the condition of extreme current and capacity of 10 mA cm^{-2} and 10 mAh cm^{-2} used), at least the safety hazard of short circuit was completely avoided here. In addition, it should be noted that the reason for a larger "polarization potential" of Li–Sb–Sn/Li–Sb–Sn cell (see Fig. 4a, the inset, the blue) was not actually all kinetic polarization potential, but also because of the multi-staged open circuit voltage (OCV) of Li–Sb–Sn electrode itself in reaction (2) [50].

For comparison of the structural integrity, the cycled Li_{BCC} metal showed visually obvious pulverization and gross mechanical delamination after deep plating/stripping of Li (Fig. 4b), but Li–Sb–Sn still kept a decent mechanical strength and integrity (see Fig. 4d). Further SEM analysis showed the initially dense Li_{BCC} foil became broken and powdered (Fig. 4c) but Li–Sb–Sn still had a relatively dense and compact structure (Fig. 4e). What is more, the Li_{BCC} foil thickened to 405 μm from the initial 200 μm (Fig. 4f, the pink), which was almost twice of Li–Sb–Sn thickening, e.g. Li–Sb–Sn thickened to 304 μm from the initial 200 μm (Fig. 4f, the green). Despite the fact that some cracks still can be found, the electrode seemed to be self-healing by organic electrolyte decomposition products [45] like glue to assist the electrode in maintaining a relatively sturdy structure (Figs. 4e and Fig. 1e).

Compared to the intensely flammable lithium metal foil, Li–Sb–Sn foil showed satisfactory air stability and fire safety [26,41]. As shown in Fig. S26, after exposed to the air for 10 h, despite the slightly darkened surface color of Li–Sb–Sn electrode, it still had capacity retention of

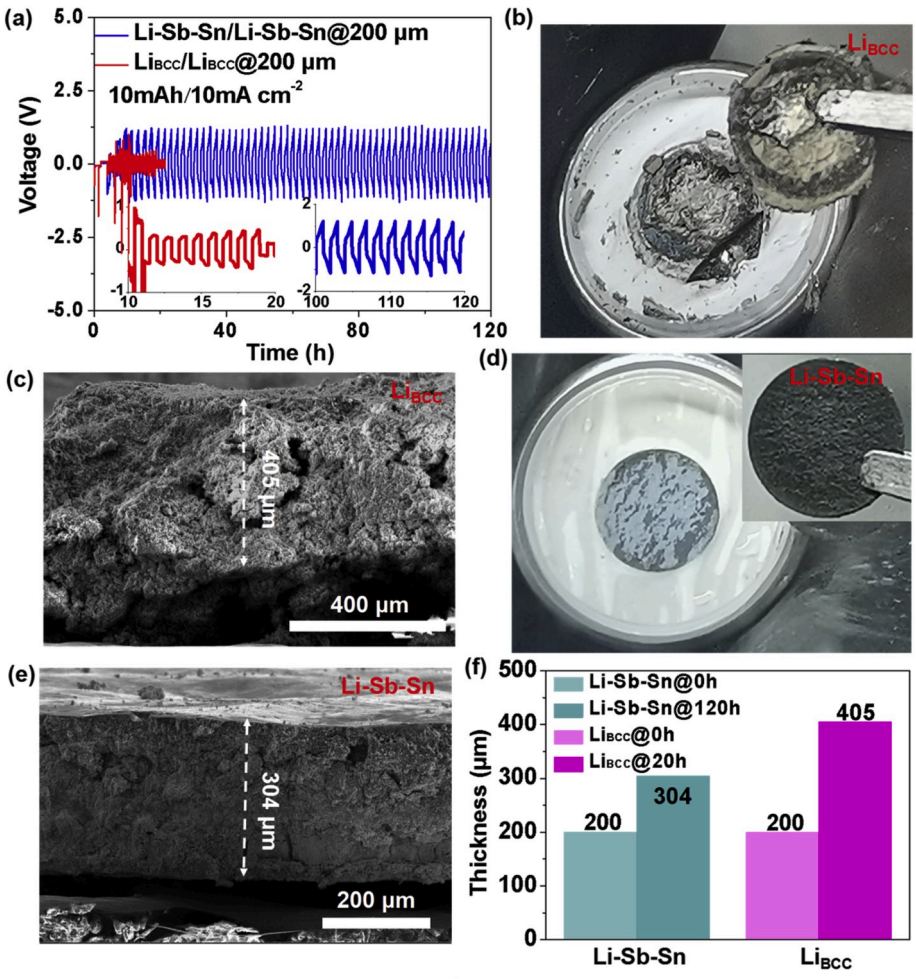

Fig. 4. Cycle life of Li–Sb–Sn/Li–Sb–Sn and Li_{BCC}/Li_{BCC} symmetrical cells during deep plating/stripping lithium. a) Voltage-Time profiles of Li–Sb–Sn/Li–Sb–Sn (the blue) and Li_{BCC}/Li_{BCC} (the red) symmetrical cells at 10 mAh cm^{-2} and 10 mA cm^{-2}. b, c) Digital photo (b) and SEM image (c) of cycled Li_{BCC} foil after 20 h. d, e) Digital photo (d) and SEM image (e) of cycled Li–Sb–Sn foil after 120 h. f) Thickness variations of cycled Li–Sb–Sn and Li_{BCC} electrodes.

93.5% (Fig. S27). The flammability of Li–Sb–Sn and Li_{BCC} electrodes (both are 100 μm) was explored by directly burning samples with alcohol lamp flame in the air. As shown in Fig. 5a and Video S1, despite the Li–Sb–Sn electrode shrank due to melting of Sn metal (the melting point of Sn is ~230 °C), the electrode itself would not burn after removing the lamp flame. In contrast, Li_{BCC} foil instantly burned out of control once in contact with a flame. As shown in Fig. 5b and Video S2, even removing the alcohol lamp, Li_{BCC} foil was still burning and shining with dazzling light.

Lastly, needle piercing experiments were performed on cycled LCO/Li–Sb–Sn (Fig. 5c and Video S3) and LCO/Li_{BCC} (Video S4) pouch cells with capacity of ~110 mAh (see Figs. S28 and S29). Although neither pouch cell caught fire after needle piercing, the LCO/Li_{BCC} pouch cell generated significantly more heat. As shown in Fig. 5d, the temperature of LCO/Li_{BCC} has risen by 2.8 °C (from 26.9 °C to 29.7 °C) after piercing, but the temperature of LCO/Li–Sb–Sn cell increased by only 0.3 °C (e.g. from 26.9 °C to 27.2 °C), which proved that Li–Sb–Sn cell was much less likely to initiate thermal runaway after short circuiting than Li_{BCC} of the same thickness. Besides, the maximum applied force of LCO/Li–Sb–Sn (Fig. 5e, the blue) during the piercing measurement was 110 N but LCO/Li_{BCC} (Fig. 5e, the orange) only sustained 80 N, which indicates LCO/Li–Sb–Sn has larger mechanical resistance to piercing.

4. Conclusions

To summarize, in this study, a self-supporting mechanically prelithiated Li–Sb–Sn foil was proved to outperform pure Li_{BCC} metal anode in multiple ways. When paired against various cathodes under limited electrolyte near the industrial level of 6–8 g (electrolyte)/Ah, Li–Sn–Sb foil achieves much better full-cell performance than Li_{BCC} anode. In particular, LCO/Li–Sb–Sn pouch cell delivers an initial volumetric energy density of 1073 Wh L^{-1} and remains 909 Wh L^{-1} after 20 cycles. Coulombic inefficiency analysis and morphological observations show the excellent full-cell performance should be attributed to the smaller volume change of Li–Sn–Sb electrode. Doping 5 wt% Sb offers extra GBs and nano SnSb PBs to relieve stress, evidenced by the smaller porosity (~11% of Li–Sn–Sb versus 23% of Li–Sn) right after mechanical prelithiation. Doping Sb also changes the reaction kinetics and lithiation products of Sn electrode due to forming nano Sn particles during lithiating SnSb particles, breaking down a huge Sn→$Li_{22}Sn_5$ shock into several milder ones Sn→Li_2Sn_5→LiSn→$Li_{22}Sn_5$ through the "lithium-poor" intermetallic phases, reducing the structural damage. Finally, Li–Sn–Sb electrode shows much better air stability, fire safety and short circuiting stability than Li_{BCC} metal anode. While the Li-carrying ability of $Li_{22}Sn_5$ is similar to that of Li_{BCC}, the unique mesoscale features (low volume expansion, no initial deep damage), cycling stability and higher

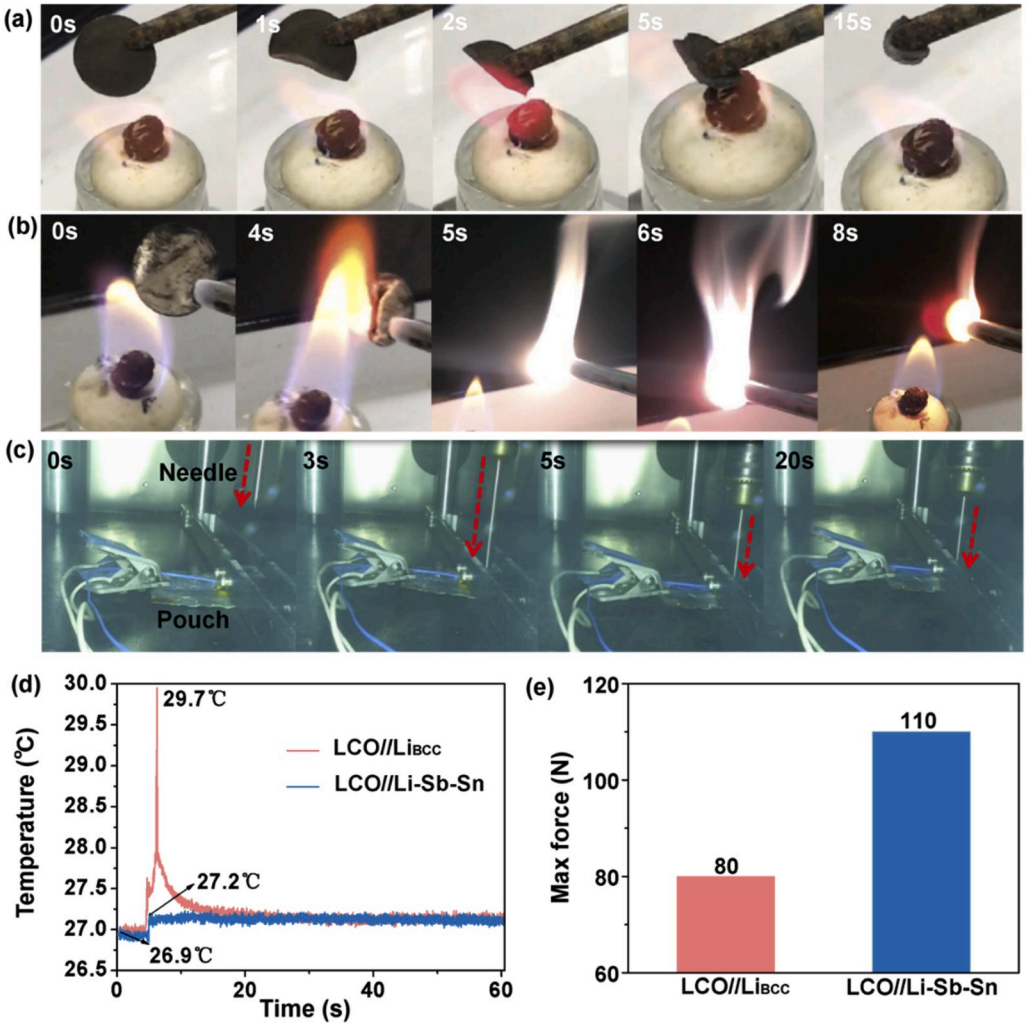

Fig. 5. Fire safety of Li–Sb–Sn electrode and needle piercing experiment of LCO/Li–Sb–Sn pouch cell. a, b) Burning 100 μm thick Li–Sn–Sb (a) and 100 μm thick Li foil (b) with flame in the air, also see Video S1, S2. c) Digital photos of LCO/Li–Sb–Sn pouch of needle piercing experiment process. Also see Video S3 and S4 for piercing experiment of LCO/Li–Sb–Sn and LCO/Li pouch cell. d) Temperature variations of LCO/Li–Sb–Sn and LCO/Li_{BCC} pouch cells during needle piercing experiment. e) Applied max force of LCO/Li–Sb–Sn and LCO/Li_{BCC} pouch cells in needle piercing experiment.

safety of prelithiated Li–Sn–Sb foil means it comprehensively surpasses Li_{BCC} metal foil anode.

Declaration of competing interest

The authors declare that they have no known competing financial interests or personal relationships that could have appeared to influence the work reported in this paper.

CRediT authorship contribution statement

Hui Xu: Conceptualization, Data curation, Formal analysis, Investigation, Writing - original draft. **Sa Li:** Conceptualization, Data curation, Formal analysis, Funding acquisition. **Xinlong Chen:** Investigation, Writing - original draft. **Can Zhang:** Investigation. **Zhuoqun Tang:** Investigation. **Huimin Fan:** Methodology. **Yue Yu:** Methodology. **Wenjian Liu:** Methodology. **Na Liang:** Methodology. **Yunhui Huang:** Conceptualization, Data curation, Formal analysis, Funding acquisition. **Ju Li:** Conceptualization, Writing - review & editing.

Acknowledgments

JL acknowledges support by Samsung Advanced Institute of Technology. The authors are grateful for the support from the National Natural Science Foundation of China (NSFC-No. 91934304, 51632001 and 51972236).

Appendix A. Supplementary data

Supplementary data to this article can be found online at https://doi.org/10.1016/j.nanoen.2020.104815.

References

[1] J. Xiang, L. Yang, L. Yuan, K. Yuan, Y. Zhang, Y. Huang, J. Lin, F. Pan, Y. Huang, Alkali-metal anodes: from lab to market, Joule 3 (2019) 2334–2363, https://doi.org/10.1016/j.joule.2019.07.027.
[2] C. Fang, X. Wang, Y.S. Meng, Key issues hindering a practical lithium-metal anode, Trends Chem. 1 (2019) 152–158, https://doi.org/10.1016/j.trechm.2019.02.015.
[3] X.B. Cheng, R. Zhang, C.Z. Zhao, Q. Zhang, Toward safe lithium metal anode in rechargeable batteries: a review, Chem. Rev. 117 (2017) 10403–10473, https://doi.org/10.1021/acs.chemrev.7b00115.

[4] B. Scrosati, J. Garche, Lithium batteries: status, prospects and future, J. Power Sources 195 (2010) 2419–2430, https://doi.org/10.1016/j.jpowsour.2009.11.048.
[5] A. Mauger, M. Armand, C.M. Julien, K. Zaghib, Challenges and issues facing lithium metal for solid-state rechargeable batteries, J. Power Sources 353 (2017) 333–342, https://doi.org/10.1016/j.jpowsour.2017.04.018.
[6] S. Li, M. Jiang, Y. Xie, H. Xu, J. Jia, J. Li, Developing high-performance lithium metal anode in liquid electrolytes: challenges and progress, Adv. Mater. 30 (2018) 1706375, https://doi.org/10.1002/adma.201706375.
[7] P. Albertus, S. Babinec, S. Litzelman, A. Newman, Status and challenges in enabling the lithium metal electrode for high-energy and low-cost rechargeable batteries, Nat. Energy 3 (2018) 16–21, https://doi.org/10.1038/s41560-017-0047-2.
[8] D. Lin, Y. Liu, Y. Cui, Reviving the lithium metal anode for high-energy batteries, Nat. Nanotechnol. 12 (2017) 194, https://doi.org/10.1038/nnano.2017.16.
[9] D. Aurbach, E. Zinigrad, Y. Cohen, H. Teller, A short review of failure mechanisms of lithium metal and lithiated graphite anodes in liquid electrolyte solutions, Solid State Ionics 148 (2002) 405–416, https://doi.org/10.1016/S0167-2738(02)00080-2.
[10] X.B. Cheng, R. Zhang, C.Z. Zhao, F. Wei, J.G. Zhang, Q. Zhang, A review of solid electrolyte interphases on lithium metal anode, Adv. Sci. 3 (2016) 1500213, https://doi.org/10.1002/advs.201500213.
[11] P. Limthongkul, Y.I. Jang, N.J. Dudney, Y.M. Chiang, Electrochemically-driven solid-state amorphization in lithium–metal anodes, J. Power Sources 119–121 (2003) 604–609, https://doi.org/10.1016/S0378-7753(03)00303-3.
[12] J. Qian, W.A. Henderson, W. Xu, P. Bhattacharya, M. Engelhard, O. Borodin, J. G. Zhang, High rate and stable cycling of lithium metal anode, Nat. Commun. 6 (2015) 6362, https://doi.org/10.1038/ncomms7362.
[13] C.M. Park, S. Yoon, S.I. Lee, J.H. Kim, J.H. Jung, H.J. Sohn, High-rate capability and enhanced cyclability of antimony-based composites for lithium rechargeable batteries, J. Electrochem. Soc. 154 (2007) A917–A920, https://doi.org/10.1149/1.2761829.
[14] R. Weber, M. Genovese, A.J. Louli, S. Hames, C. Martin, I.G. Hill, J.R. Dahn, Long cycle life and dendrite-free lithium morphology in anode-free lithium pouch cells enabled by a dual-salt liquid electrolyte, Nat. Energy 4 (2019) 683–689, https://doi.org/10.1038/s41560-019-0428-9.
[15] X. Guan, A. Wang, S. Liu, G. Li, F. Liang, Y.W. Yang, X. Liu, J. Luo, Controlling nucleation in lithium metal anodes, Small 14 (2018) 1801423, https://doi.org/10.1002/smll.201801423.
[16] L. Suo, W. Xue, M. Gobet, S.G. Greenbaum, C. Wang, Y. Chen, W. Yang, Y. Li, J. Li, Fluorine-donating electrolytes enable highly reversible 5-V-class Li metal batteries, Proc. Natl. Acad. Sci. 115 (2018) 1156, https://doi.org/10.1073/pnas.1712895115.
[17] G. Zheng, S.W. Lee, Z. Liang, H.W. Lee, K. Yan, H. Yao, H. Wang, W. Li, S. Chu, Y. Cui, Interconnected hollow carbon nanospheres for stable lithium metal anodes, Nat. Nanotechnol. 9 (2014) 618–623, https://doi.org/10.1038/nnano.2014.152.
[18] M. Winter, J.O. Besenhard, M.E. Spahr, P. Novák, Insertion electrode materials for rechargeable lithium batteries, Adv. Mater. 10 (1998) 725–763, https://doi.org/10.1002/(SICI)1521-4095(199807).
[19] M. Winter, J.O. Besenhard, Electrochemical lithiation of tin and tin-based intermetallics and composites, Electrochim. Acta 31 (2010) 31–50, https://doi.org/10.1002/chin.200003257.
[20] S. Yang, P.Y. Zavalij, M.S. Whittingham, Anodes for lithium batteries: tin revisited, Electrochem. Commun. 5 (2003) 587–590, https://doi.org/10.1016/S1388-2481(03)00135-8.
[21] C.M. Park, J.H. Kim, H. Kim, H.J. Sohn, Li-alloy based anode materials for Li secondary batteries, Chem. Soc. Rev. 39 (2010) 3115–3141, https://doi.org/10.1039/B919877F.
[22] N. Nitta, G. Yushin, High-capacity anode materials for lithium-ion batteries: choice of elements and structures for active particles, Part. Part. Syst. Char. 31 (2014) 317–336, https://doi.org/10.1002/ppsc.201300231.
[23] J. Zhao, G. Zhou, K. Yan, J. Xie, Y. Li, L. Liao, Y. Jin, K. Liu, P.C. Hsu, J. Wang, H. M. Cheng, Y. Cui, Air-stable and freestanding lithium alloy/graphene foil as an alternative to lithium metal anodes, Nat. Nanotechnol. 12 (2017) 993, https://doi.org/10.1038/nnano.2017.129.
[24] D. Larcher, S. Beattie, M. Morcrette, K. Edström, J.C. Jumas, J.M. Tarascon, Recent findings and prospects in the field of pure metals as negative electrodes for Li-ion batteries, J. Mater. Chem. 17 (2007) 3759–3772, https://doi.org/10.1039/B705421C.
[25] J. Chen, Recent progress in advanced materials for lithium ion batteries, Materials 6 (2013) 156–183, https://doi.org/10.3390/ma6010156.
[26] H. Xu, S. Li, C. Zhang, X. Chen, W. Liu, Y. Zheng, Y. Xie, Y. Huang, J. Li, Roll-to-roll prelithiation of Sn foil anode suppresses gassing and enables stable full-cell cycling of lithium ion batteries, Energy Environ. Sci. 12 (2019) 2991–3000, https://doi.org/10.1039/C9EE01404G.
[27] H. Liu, X.B. Cheng, J.Q. Huang, S. Kaskel, S. Chou, H.S. Park, Q. Zhang, Alloy anodes for rechargeable alkali-metal batteries: progress and challenge, ACS Mater. Lett. 1 (2019) 217–229, https://doi.org/10.1021/acsmaterialslett.9b00118.
[28] X.B. Cheng, H.J. Peng, J.Q. Huang, F. Wei, Q. Zhang, Dendrite-free nanostructured anode: entrapment of lithium in a 3D fibrous matrix for ultra-stable lithium–sulfur batteries, Small 10 (2014) 4257–4263, https://doi.org/10.1002/smll.201401837.
[29] S. Lu, Z. Wang, H. Yan, R. Wang, K. Lu, Y. Cheng, W. Qin, X. Wu, High rate and cycling stable Li metal anodes enabled with aluminum-zinc oxides modified copper foam, J. Energy Chem. 41 (2020) 87–92, https://doi.org/10.1016/j.jechem.2019.04.024.
[30] X. Guo, L. Zhang, Y. Ding, J.B. Goodenough, G. Yu, Room-temperature liquid metal and alloy systems for energy storage applications, Energy Environ. Sci. 12 (2019) 2605–2619, https://doi.org/10.1039/C9EE01707K.
[31] S. Yang, P.Y. Zavalij, M. Stanley Whittingham, Sn and SnBi foil as anode materials for secondary lithium battery, MRS Proceedings 756 (2011), https://doi.org/10.1557/PROC-756-EE8.4. EE8.4.
[32] J. Yang, Y. Takeda, N. Imanishi, J.Y. Xie, O. Yamamoto, Intermetallic $SnSb_x$ compounds for lithium insertion hosts, Solid State Ionics 133 (2000) 189–194, https://doi.org/10.1016/S0167-2738(00)00749-9.
[33] S. Das, T.N. Guru Row, A.J. Bhattacharyya, Probing the critical role of Sn content in SnSb@c nanofiber anode on Li storage mechanism and battery performance, ACS Omega 2 (2017) 9250–9260, https://doi.org/10.1021/acsomega.7b01479.
[34] S. Jena, A. Mitra, A. Patra, S. Sengupta, K. Das, S.B. Majumder, S. Das, Sandwich architecture of Sn-SnSb alloy nanoparticles and N-doped reduced graphene oxide sheets as a high rate capability anode for lithium-ion batteries, J. Power Sources 401 (2018) 165–174, https://doi.org/10.1016/j.jpowsour.2018.08.058.
[35] R. Benedek, M.M. Thackeray, Lithium reactions with intermetallic-compound electrodes, J. Power Sources 110 (2002) 406–411, https://doi.org/10.1016/S0378-7753(02)00204-5.
[36] F. Rao, Z. Song, K. Ren, X. Li, L. Wu, W. Xi, B. Liu, $Sn_{12}Sb_{88}$ material for phase change memory, Appl. Phys. Lett. 95 (2009), 032105, https://doi.org/10.1063/1.3184787.
[37] Q. Ru, Q. Tian, S.-j. Hu, L.-z. Zhao, Lithium intercalation mechanism for β-SnSb in Sn-Sb thin films, Int. J. Miner. Metall. Mater. 18 (2011) 216–222, https://doi.org/10.1007/s12613-011-0425-x.
[38] S.C. Chao, Y.F. Song, C.C. Wang, H.S. Sheu, H.C. Wu, N.L. Wu, Study on microstructural deformation of working Sn and SnSb anode particles for Li-ion batteries by in situ transmission X-ray microscopy, J. Phys. Chem. C 115 (2011) 22040–22047, https://doi.org/10.1021/jp206829q.
[39] M. Prieler, H.G. Bohn, W. Schilling, H. Trinkaus, Grain boundary sliding in thin substrate-bonded Al films, J. Alloys Compd. 211–212 (1994) 424–427, https://doi.org/10.1016/0925-8388(94)90536-3.
[40] V.V. Astanin, S.N. Faizova, K.A. Padmanabhan, Model for grain boundary sliding and its relevance to optimal structural superplasticity part 2 – evidence for cooperative grain/interphase boundary sliding and plane interface formation, Mater. Sci. Technol. 12 (1996) 489–494, https://doi.org/10.1179/mst.1996.12.6.489.
[41] Y. Yu, S. Li, H. Fan, H. Xu, M. Jiang, Y. Huang, J. Li, Optimal annealing of Al foil anode for prelithiation and full-cell cycling in Li-ion battery: the role of grain boundaries in lithiation/delithiation ductility, Nano Energy 67 (2020) 104274, https://doi.org/10.1016/j.nanoen.2019.104274.
[42] S. Choi, T.w. Kwon, A. Coskun, J.W. Choi, Highly elastic binders integrating polyrotaxanes for silicon microparticle anodes in lithium ion batteries, Science 357 (2017) 279, https://doi.org/10.1126/science.aal4373.
[43] H. Xu, S. Li, X. Chen, C. Zhang, W. Liu, H. Fan, Y. Yu, Y. Huang, J. Li, Sn-alloy foil electrode with mechanical prelithiation: full-cell performance up to 200 cycles, Adv. Energy Mater. (2019), 1902150, https://doi.org/10.1002/aenm.201902150.
[44] H. Fan, B. Chen, S. Li, Y. Yu, H. Xu, M. Jiang, Y. Huang, J. Li, Nanocrystalline Li–Al–Mn–Si foil as reversible Li host: electronic percolation and electrochemical cycling stability, Nano Lett. 20 (2020) 896–904, https://doi.org/10.1021/acs.nanolett.9b03626.
[45] Y. Jin, S. Li, A. Kushima, X. Zheng, Y. Sun, J. Xie, J. Sun, W. Xue, G. Zhou, J. Wu, F. Shi, R. Zhang, Z. Zhu, K. So, Y. Cui, J. Li, Self-healing SEI enables full-cell cycling of a silicon-majority anode with a coulombic efficiency exceeding 99.9%, Energy Environ. Sci. 10 (2017) 580–592, https://doi.org/10.1039/C6EE02685K.
[46] I.A. Courtney, J.S. Tse, O. Mao, J. Hafner, J.R. Dahn, Ab initio calculation of the lithium-tin voltage profile, Phys. Rev. B 58 (1998) 15583–15588, https://doi.org/10.1103/PhysRevB.58.15583.
[47] R. Xu, X.B. Cheng, C. Yan, X.Q. Zhang, Y. Xiao, C.Z. Zhao, J.Q. Huang, Q. Zhang, Artificial interphases for highly stable lithium metal anode, Matter 1 (2019) 317–344, https://doi.org/10.1016/j.matt.2019.05.016.
[48] Y. Yuan, F. Wu, G. Chen, Y. Bai, C. Wu, Porous LiF layer fabricated by a facile chemical method toward dendrite-free lithium metal anode, J. Energy Chem. 37 (2019) 197–203, https://doi.org/10.1016/j.jechem.2019.03.014.
[49] R. Xu, Y. Xiao, R. Zhang, X.B. Cheng, C.Z. Zhao, X.Q. Zhang, C. Yan, Q. Zhang, J. Q. Huang, Dual-phase single-ion pathway interfaces for robust lithium metal in working batteries, Adv. Mater. 31 (2019) 1808392, https://doi.org/10.1002/adma.201808392.
[50] C.J. Wen, R.A. Huggins, Chemical diffusion in intermediate phases in the lithium-tin system, J. Solid State Chem. 35 (1980) 376–384, https://doi.org/10.1016/0022-4596(80)90535-6.

Hui Xu is currently a Ph.D. candidate in School of Materials Science and Engineering at Tongji University. Her researches mainly focus on advanced Sn-based and lithium metal anodes for high-energy-density storage devices.

Sa Li received her Ph.D. degree in Materials Science and Engineering from Tsinghua University in 2015. Afterwards, she joined the School of Materials Science and Engineering at Tongji University as an assistant professor until now. Her current research interest is mainly on designing advanced anode and cathode materials for lithium-ion batteries, Li–S batteries.

Xinlong Chen is currently an undergraduate student in School of Materials Science and Engineering at Tongji University. His researches mainly focus on high-performance alloy anodes for lithium ion batteries and sodium ion batteries.

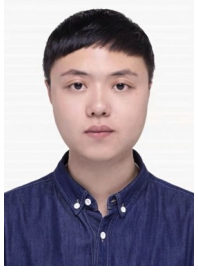

Can Zhang is currently an undergraduate student in School of Materials Science and Engineering at Tongji University. His researches mainly focus on high-performance alloy anodes and lithium anodes for lithium ion batteries.

Zhuoqun Tang is currently a Master student in School of Materials Science and Engineering at Tongji University. Her research interest is mainly on lithium metal anode materials for high-energy-density lithium batteries.

Huimin Fan is currently a PhD student in School of Materials Science and Engineering at Tongji University. Her researches mainly focus on advanced electrode materials for energy storage devices, such as Al, Sn anodes and lithium metal batteries.

Yue Yu is currently a Master student in School of Materials Science and Engineering at Tongji University. His research mainly focused on advanced anode materials for Li-ion batteries.

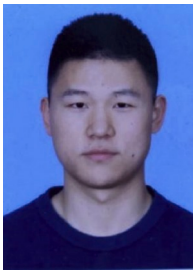

Wenjian Liu is currently an undergraduate student in School of Materials Science and Engineering at Tongji University. His researches mainly focus on anodes materials for Li-ion/Na-ion batteries.

Na Liang is a Master student in School of Materials Science and Engineering at Tongji University. Her research is mainly focuses on advanced anode materials for Li ion batteries.

Yunhui Huang received his Ph.D. from Peking University in 2000. From 2004 to 2007, he worked with Prof. John Goodenough in the University of Texas at Austin. In 2008, he became a Chair Professor of materials science in Huazhong University of Science and Technology. He is now the Director of the Institute of New Energy for Vehicles in Tongji University. His research group works on rechargeable batteries for energy storage and their electrode materials.

Ju Li is BEA Professor of Nuclear Science and Engineering and Professor of Materials Science and Engineering at MIT. His group (http://Li.mit.edu) performs computational and experimental research on mechanical properties of materials, and energy storage and conversion. Ju was elected Fellow of the American Physical Society in 2014 and Fellow of the Materials Research Society in 2017.

Supplementary Information

Surpassing lithium metal rechargeable batteries with self-supporting Li-Sn-Sb foil anode

Hui Xu, Sa Li*, Xinlong Chen, Can Zhang, Zhuoqun Tang, Huimin Fan, Yue Yu, Wenjian Liu, Na Liang, Yunhui Huang* and Ju Li*

[1]School of Materials Science and Engineering, Tongji University, Shanghai 201804, China
[2]Institute of New Energy for Vehicles, Tongji University, Shanghai 201804, China
[3]Department of Nuclear Science and Engineering and Department of Materials Science and Engineering, Massachusetts Institute of Technology, Cambridge, MA 02139, USA
†These authors contributed equally to this work

*Corresponding authors
Email address: lisa@tongji.edu.cn; huangyh@tongji.edu.cn; liju@mit.edu

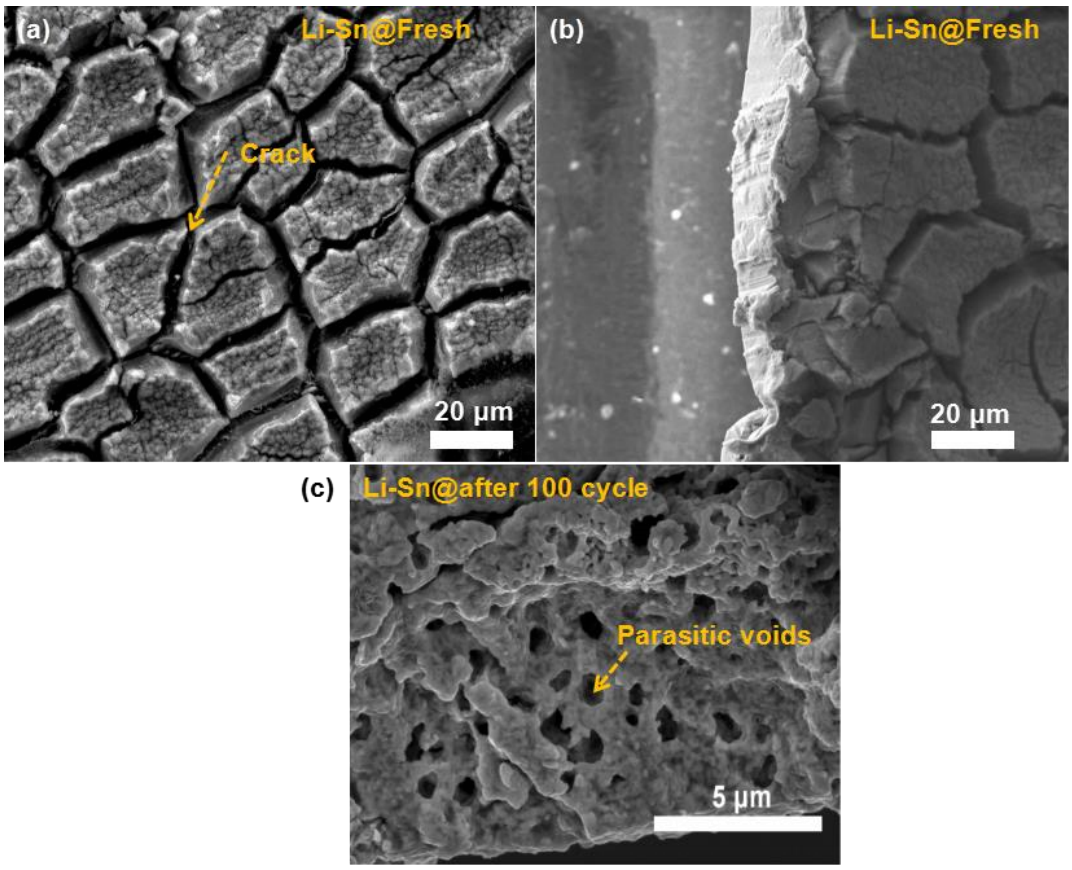

Fig. S1. SEM images of cracks and parasitic voids in Li-Sn electrode. a, b) Cracks in the fresh Li-Sn electrode prepared by MP. The cracks formation is due to the large volume change and stress releasing during the mechanical prelithiation. c) Parasitic voids of cycled Li-Sn electrode, caused by volume change and recrystallization of Sn matrix, as well as the corrosion of electrolyte during electrochemically cycling.

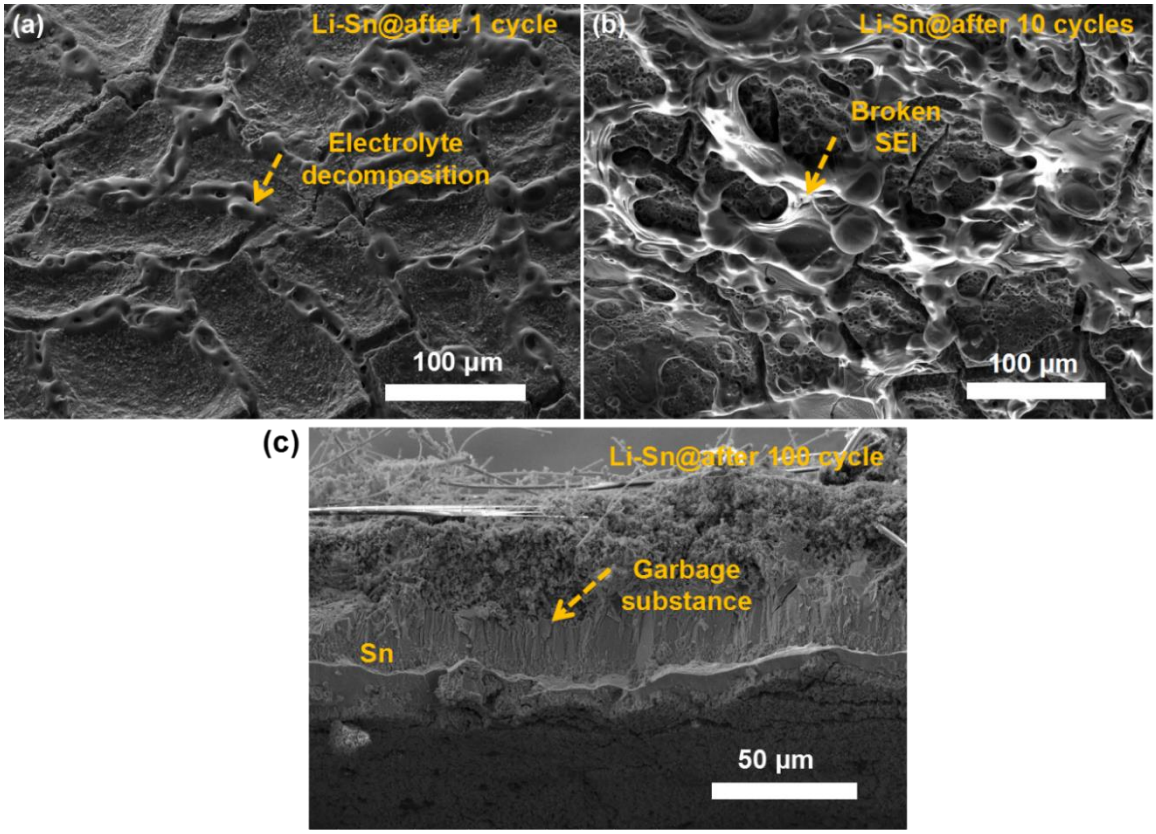

Fig. S2. SEM images of electrode thickening caused by the accumulation of electrolyte decomposition products. a) SEM image of Li-Sn electrode just after 1 cycle. The liquid electrolyte permeated and decomposed along cracks. b) The broken SEI covered on the electrode surface. The electrode was observed after 10 cycles. c) SEM image of Li-Sn electrode cycled 100 cycles. The garbage substance, including electrolyte decomposition and inactive electrode fragments, accumulated on the electrode surface and resulted in an evident electrode thickening.

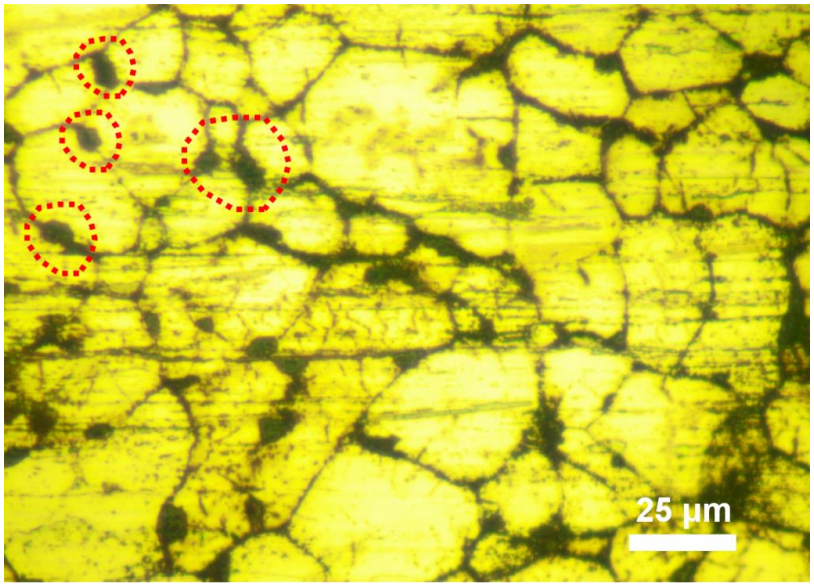

Fig. S3. Digital photo of precipitated SnSb particles in the etched 5wt%Sb-95wt%Sn foil. The black particles circled by the red dotted line are SnSb particles.

Element	Wt%	At%
CK	02.53	13.80
OK	09.28	38.03
SnL	50.83	28.07
SbL	37.35	20.11
Matrix	Correction	ZAF

Fig. S4. EDS element analysis of the protruding particles in 5wt%Sb-95wt%Sn foil.

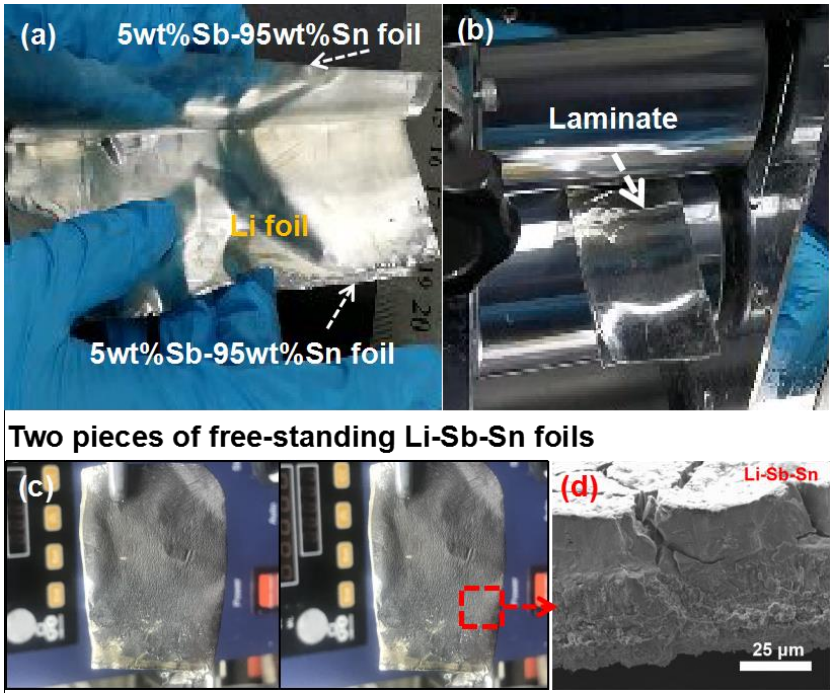

Fig. S5. Operation processes of mechanical prelithiation. a) Two 5wt%Sb-95wt%Sn foils sandwich a Li foil in the middle. b) After pressing, lithium will be fully 'absorbed' into Sn-based foils and a laminate will form. c) The as-formed laminate could be separated into two pieces of identical free-standing Li-Sb-Sn foils by mechanical peeling very easily. d) Each piece of Li-Sb-Sn foil is consisted of a part of lithiated porous and residual dense 5wt%Sb-95wt%Sn matrix.

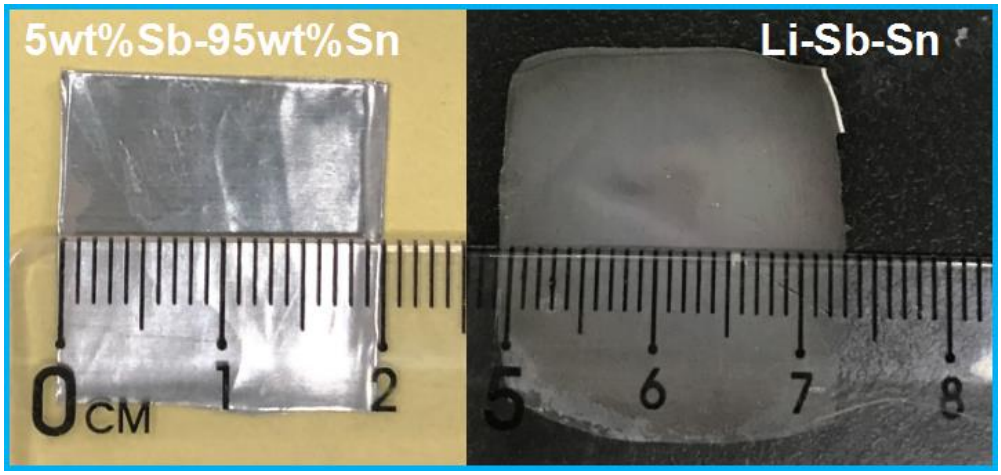

Fig. S6. Dimension size measurements of 5wt%Sb-95wt%Sn foil before and after mechanical prelithiation.

After prelithiation, the area of foil expanded to 5.75 cm^2 = 2.5 cm × 2.3 cm (the right) from the initial 4 cm^2 = 2 cm × 2 cm of 5wt%Sb-95wt%Sn foil (the left). Based on the following formula of lateral areal expansion:

$$\alpha \equiv \text{area(after MP)} / \text{area(before MP)} \qquad \text{(S1)}$$

So the lateral areal expansion α of Li-Sb-Sn is 144%. All details are listed in the following Tab. S1.

Tab. S1. Dimension size of 5wt%Sb-95wt%Sn foil before and after MP

Sample	**5wt%Sb-95wt%Sn**
Size (cm, Before MP)	2×2
Size (cm, After MP)	2.5×2.3
Lateral areal expansion	144%
α	1.44

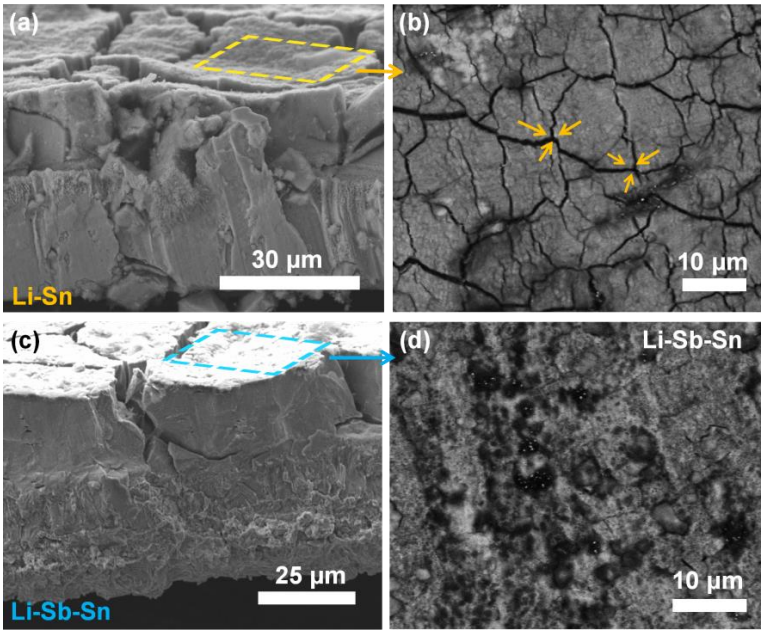

Fig. S7. SEM observation of Li-Sn and Li-Sb-Sn electrode damage. a) Li-Sn from top to bottom widely distributes deep cracks indicating severe damage. b) The evident Y-shaped second cracks on the shard. c, d) Li-Sb-Sn electrode has less damage than Li-Sn.

The more serious damage of Li-Sn directly leads to the electrical conductivity deterioration. Because this damage destroys electronic path connectivity by splitting the originally adjacent conductive grain/grain clusters, see Fig. S7a and S7b. Our previous works have revealed the metal/metal GB/PB can release stress and maintain conductivity, like the stretchable binder and conductive agent of tradition electrode. For example, silver, copper-doped Sn foil[1] or Mn, Si-doped Al foil[2] with more abundant GB/PBs has less damage and better electrical conductivity. Thus, compared to the severely damaged Li-Sn, Li-Sb-Sn has less damage (see Fig. S7c) and almost no secondary cracks on the shard (Fig. S7d)

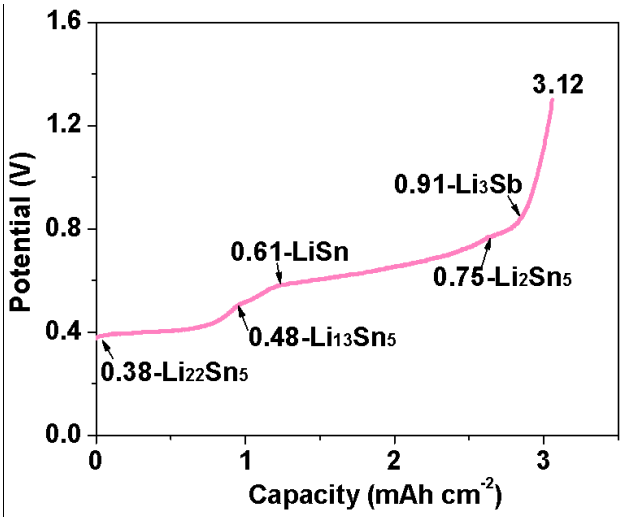

Fig. S8. Retrievable lithium inventory in Li-Sb-Sn foil electrode. 50 μm Li-Sb-Sn was prepared by rolling two 50 μm 5wt%Sb-95wt%Sn foils sandwiching 50 μm Li_{BCC} foil in the middle. The lithium inventory was determined by delithiating Li-Sb-Sn/Li_{BCC} cell to 1.5 V at a current density of 0.3 mA cm^{-2}.

Since the electrochemical reactions between Sn and Li are multi-step, multiple plateaus are

shown on the potential. With delithiation proceeding, Li-Sb-Sn foil gradually becomes lithium-poor phases from the initial lithium-rich $Li_{22}Sn_5$, proceeding as follows,

$$Li_{22}Sn_5 \rightarrow Li_xSn + (4.4\text{-}x)\ Li^+ + (4.4\text{-}x)\ e^-\ (\sim 0.4\text{-}0.8\ V\ vs.\ Li/Li^+\ (0<x<4.4)$$

According to the reaction potentials of Li–Sn compounds in **Tab. S2**,

Tab. S2. Theoretical capacities and reaction potentials of Li–Sn compounds[3,4]

	Theoretical capacity (mAh g^{-1})	**Potential (V *vs.* Li/Li^+)**
Li_2Sn_5	88.3	0.760
LiSn	213.3	0.660
Li_3Sn_2	-	-
Li_5Sn_2	492.5	0.485
$Li_{13}Sn_5$	509.6	0.485
Li_7Sn_2	656	0.420
Li_4Sn	-	-
$Li_{22}Sn_5$	790	0.380

Therefore, the electrochemical reactions at discharge plateaus respectively would proceed as:

At ~0.38 V-0.48 V (*vs.* Li/Li^+), $Li_{22}Sn_5$ changes to $Li_{13}Sn_5$ or Li_5Sn_2

$$Li_{22}Sn_5 \rightarrow Li_xSn + xe^-\ (13/5 \leqq x<22/5)$$

At ~0.48 V-0.6 V (*vs.* Li/Li^+), $Li_{13}Sn_5$ or Li_5Sn_2 changes to LiSn

$$Li_{13}Sn_5 \rightarrow Li_ySn + ye^-\ (1 \leqq y<13/5)$$

At ~0.6 V-0.7 V (*vs.* Li/Li^+), LiSn changes to lithium-poor Li_2Sn_5,

$$LiSn \rightarrow Li_zSn + ze^-\ (0.4 \leqq z<1)$$

Additionally, ~0.9 V (*vs.* Li/Li^+) is the delithiation potential of Li_3Sb, so the electrochemical reactions at ~0.92 V would proceed as:

$$Li_3Sb \rightarrow 3Li + 3e^- + Sb$$

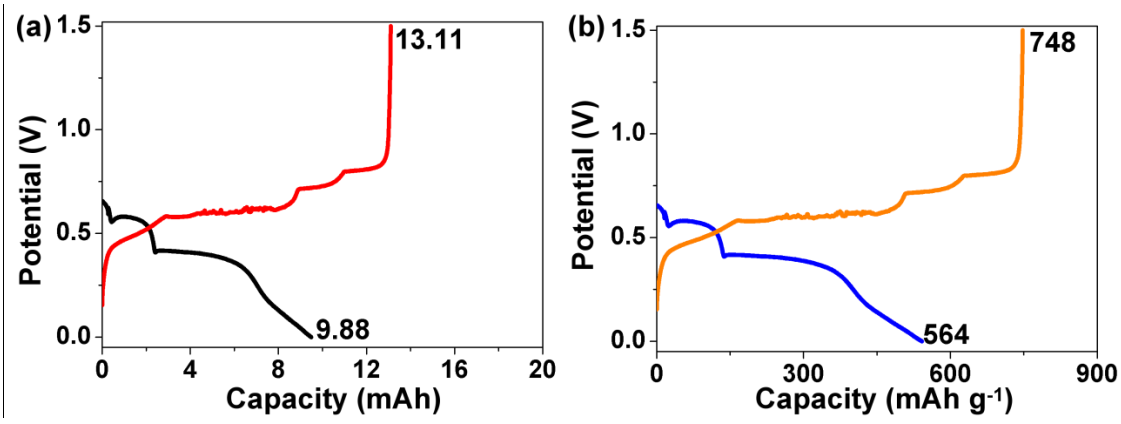

Fig. S9. Capacity and specific capacity of Li-Sb-Sn electrode. a) The biggest lithiation (the black) and delithiation (the red) capacity of Li-Sb-Sn. b) The biggest gravimetric lithiation (the blue) and delithiation (the orange) specific capacity of Li-Sb-Sn.

To determine the biggest gravimetric specific capacity of Li-Sb-Sn electrode itself, a Li-Sb-Sn/Li half-cell was assembled by adopting a Li-Sb-Sn electrode with diameter of 12 mm and weight of 17.52 mg. The half-cell was lithiated to 0 V and then delithiated to 1.5 V at

~0.88 mA cm^{-2}. As shown in Fig. S9a and S9b, the lithiation capacity of Li-Sb-Sn was 9.88 mAh and the corresponding specific capacity was ~563.92 mAh g^{-1} (= 9.88 mAh/ (17.52×10^{-3})). Furthermore, due to prelithiation treatments, the delithiation capacity of Li-Sb-Sn was higher, e.g., 13.11 mAh and ~748.29 mAh g^{-1} (= 13.11 mAh/ (17.52×10^{-3})).

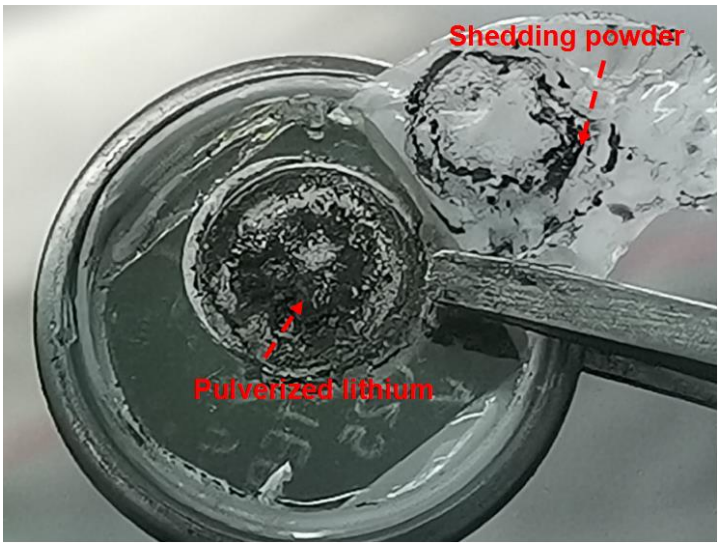

Fig. S10. Digital photo of cycled Li_{BCC} electrode from LFP/Li_{BCC} cell. The initial Li_{BCC} foil is ~50 μm thick. Just after 37 cycles, the electrolyte is drought and lithium metal is obviously pulverized and shedding.

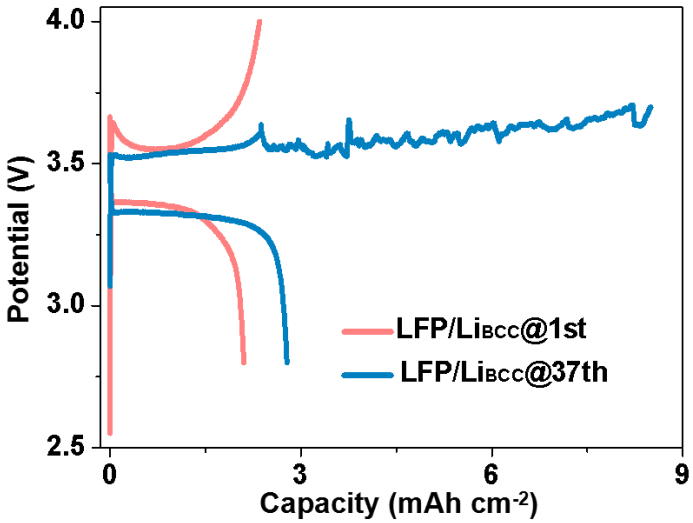

Fig. S11. Potential-Capacity profiles of LFP/Li_{BCC} cell with electrolyte of 20 μL. The orange is the 1st cycle and the blue is the 37th cycle. The charge potential of 37th cycle is fluctuating and unstable, with the cell failing to reach the cutoff voltage 3.8 V due to electrolyte drought and contamination.

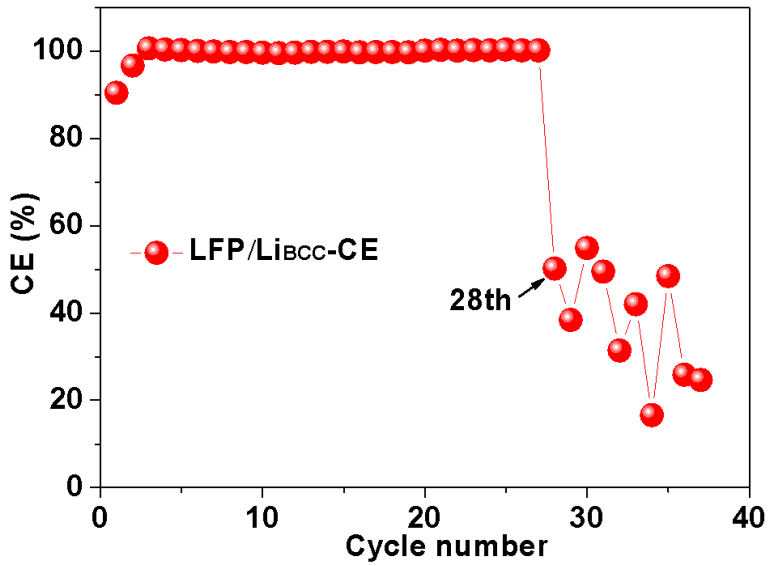

Fig. S12. Coulombic efficiency (CE) analysis of LFP/Li_{BCC} cell with 20 μL electrolyte. The 28th CE promptly dropped to ~50 % and then the later CE remained at ~50% or less.

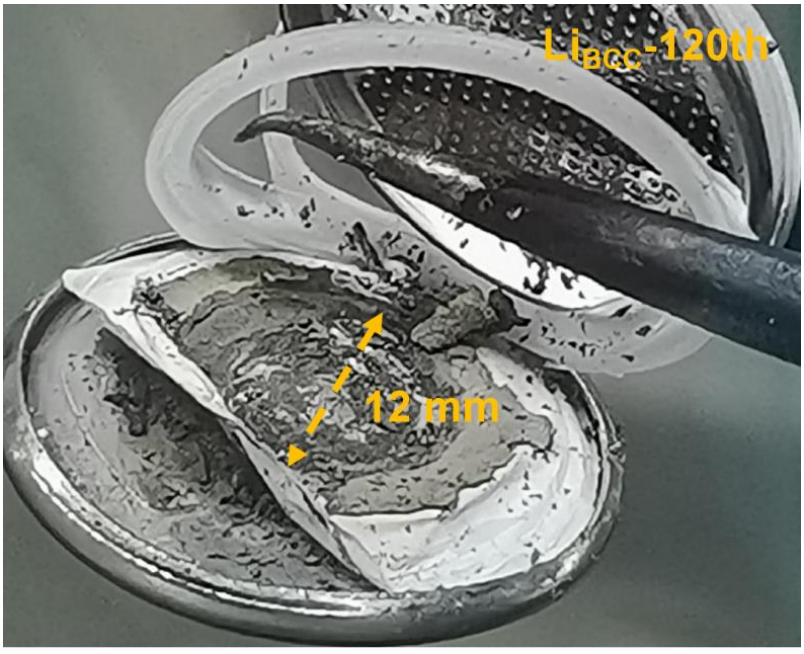

Fig. S13. Digital photo of the cycled Li_{BCC} metal foil in the LFP/Li_{BCC} cell. The 50 μm thick lithium metal foil seriously pulverized after 120 cycles.

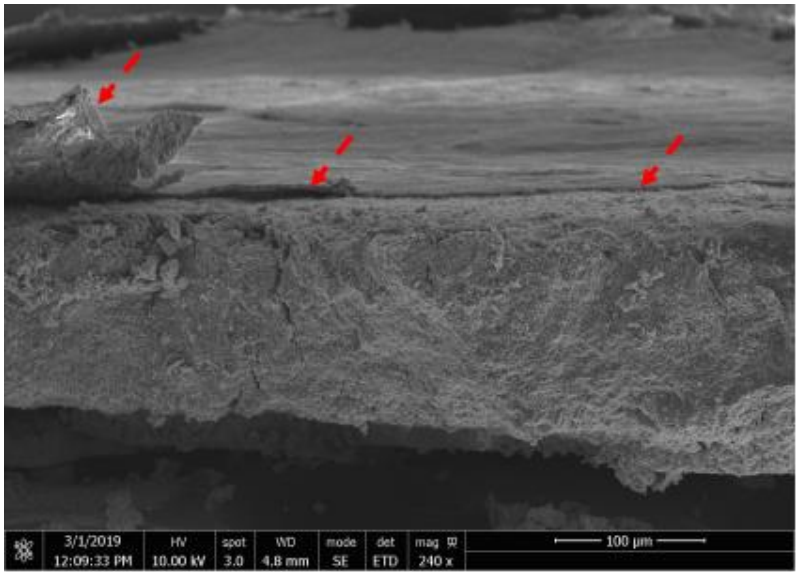

Fig. S14. SEM image of Li-Sn-Sb electrode after 200 cycles. From the cross-sectional image, the surface has a layer of dense and curled film (marked with red arrow) that can effectively prevent liquid electrolyte leakage. The formation and maintenance of dense film conversely indicates that Li-Sn-Sb electrode is stable and less of volume change during cycling process.

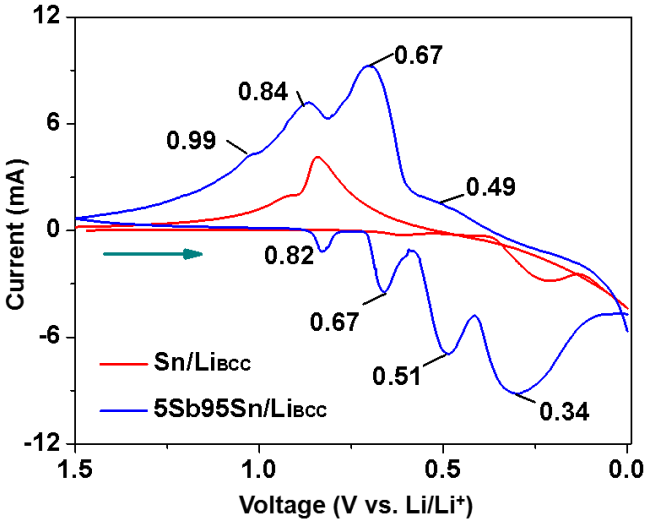

Fig. S15. CV measurements determined that the different lithiation plateaus and products in 5wt%Sb-95wt%Sn/Li_{BCC} (the blue) and Sn/Li_{BCC} cell (the red). The CV measurements were performed from 1.5 to 0 V at a current density of 0.1 mAh cm^{-2}.

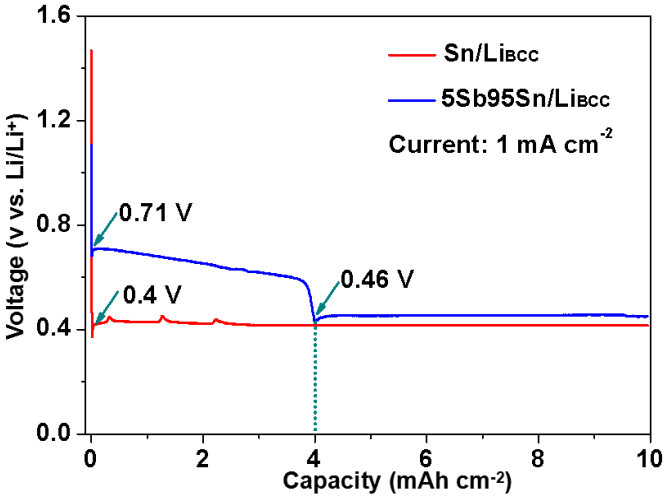

Fig. S16. Lithiation profiles of 5wt%Sb-95wt%Sn/Li_{BCC} (the blue) and Sn/Li_{BCC} (the red) at a current of 1 mA cm^{-2}. Once the lithiation starts, the potential of Sn/Li_{BCC} directly drops to 0.4 V and forms lithium-rich phase $Li_{22}Sn_5$. However, 5wt%Sb-95wt%Sn/Li_{BCC} has an evident inclined plateau between 0.71 V and 0.46 V, forming lithium-poor Li_2Sn_5 and LiSn, which totally contributes to a capacity of ~ 4 mAh cm^{-2}. Then the potential remains at ~0.46 V stably, where mainly forms lithium-rich phase $Li_{22}Sn_5$.

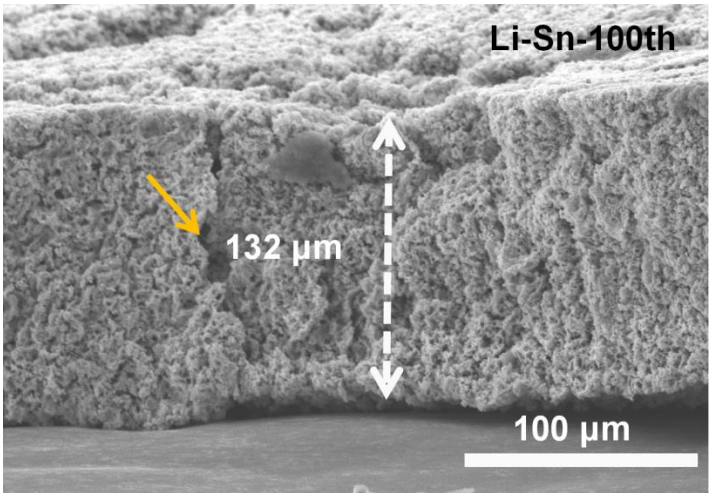

Fig. S17. Electrode expansion of Li-Sn after full-cell cycling.

After only 100 cycles, Li-Sn foil reacted deeply from the top to bottom and became loose, porous. Correspondingly, Li-Sn thickened by ~ 86 μm from the initial 46.05 μm to 132 μm. However, even after performing 200 cycles, Li-Sb-Sn has a denser structure and only thickens by 55 μm (e.g. from 50 μm to 105 μm) due to a series of "lithium-poor" intermediate phase transformations Sn → Li_2Sn_5 → LiSn → $Li_{22}Sn_5$, that reduce the "electrochemical shock" damage to the foil.

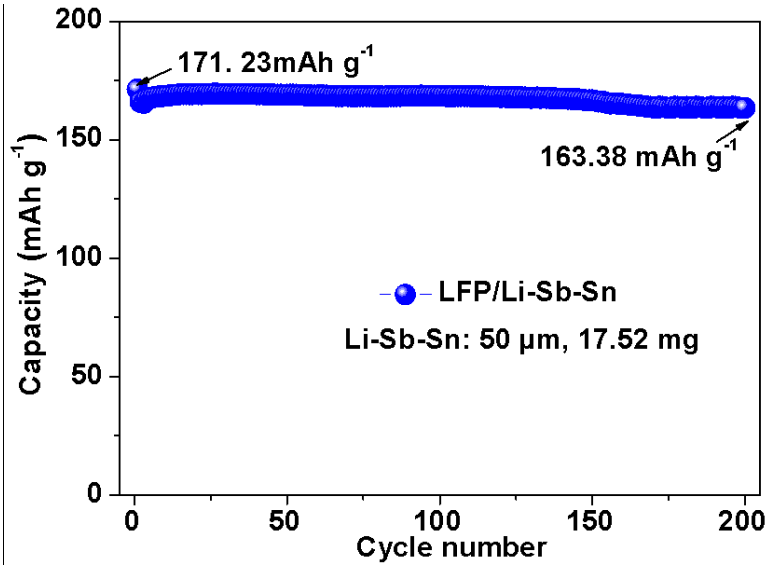

Fig. S18. Gravimetric capacity of Li-Sb-Sn electrode in a ~ 3 mAh LFP/Li-Sb-Sn cell.

According to weighing, the mass of 50 μm thick Li-Sb-Sn electrode with a diameter of 12 mm is ~17.52 mg. Thus, in a ~3 mAh LFP/Li-Sb-Sn full cell, as shown in Fig. S18, the gravimetric capacity of Li-Sb-Sn is ~171.23 mAh g^{-1} (=3 mAh/(17.52×10^{-3} g)). Evidently, the low-capacity-density LFP cathode limits the gravimetric capacity of Li-Sb-Sn. Thus, as a high-volumetric-capacity anode, Li-Sb-Sn is more suitable to pair against NCM811 and LCO cathodes.

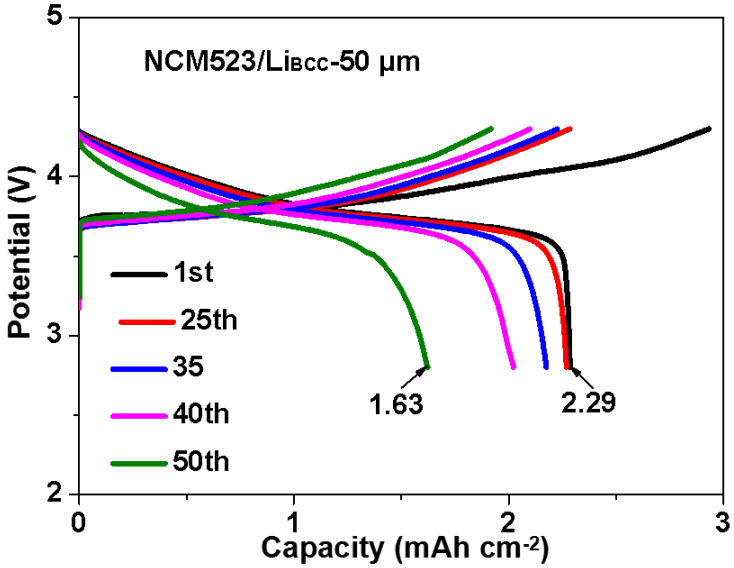

Fig. S19. Potential-Capacity profiles of NCM523/Li_{BCC} cell. The cell shows evident and continuous capacity decay. The capacity retention of 50th cycle is low to 71.18% = (1.63/2.29) × 100%.

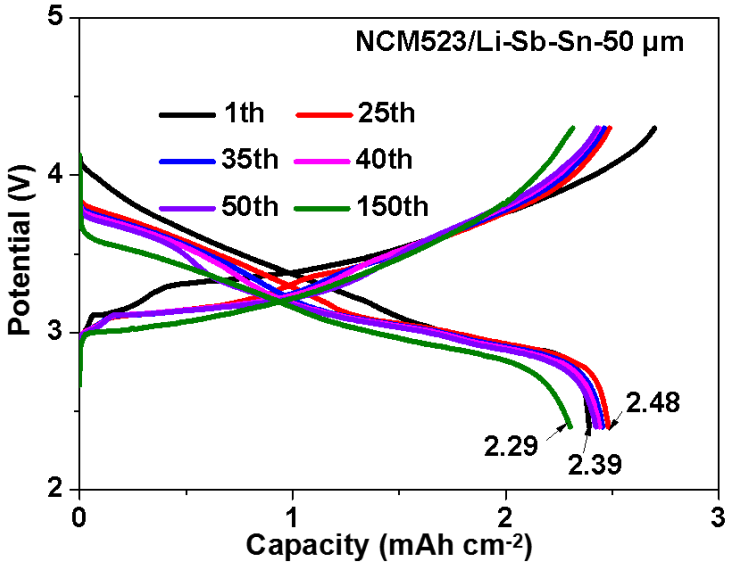

Fig. S20. Potential-Capacity profiles of NCM523/Li-Sb-Sn full cell. The capacity retention of 150th cycle is up to 95.82% = (2.29/2.39) × 100%. At first cycles, the capacity had slight increase, e.g. the capacity of 25th cycle increased to ~2.48 mAh cm^{-2} from 2.39 mAh cm^{-2} of 1st cycle.

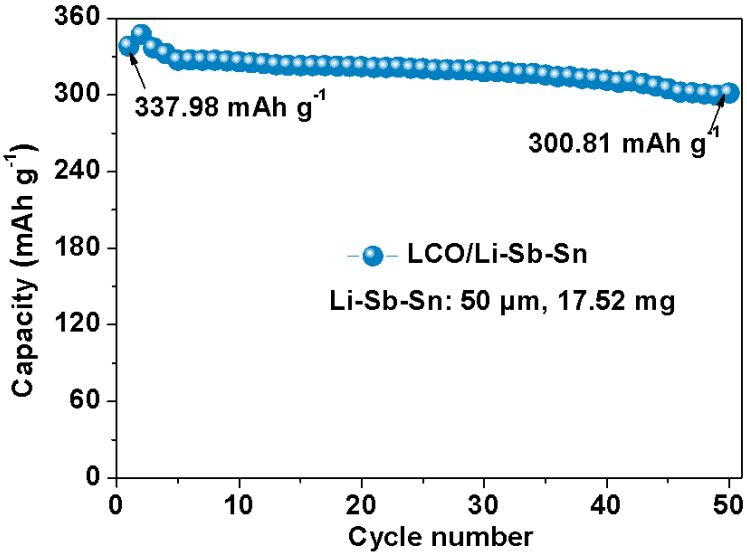

Fig. S21. Gravimetric capacity of Li-Sb-Sn electrode in a ~ 6 mAh LCO/Li-Sb-Sn full cell.

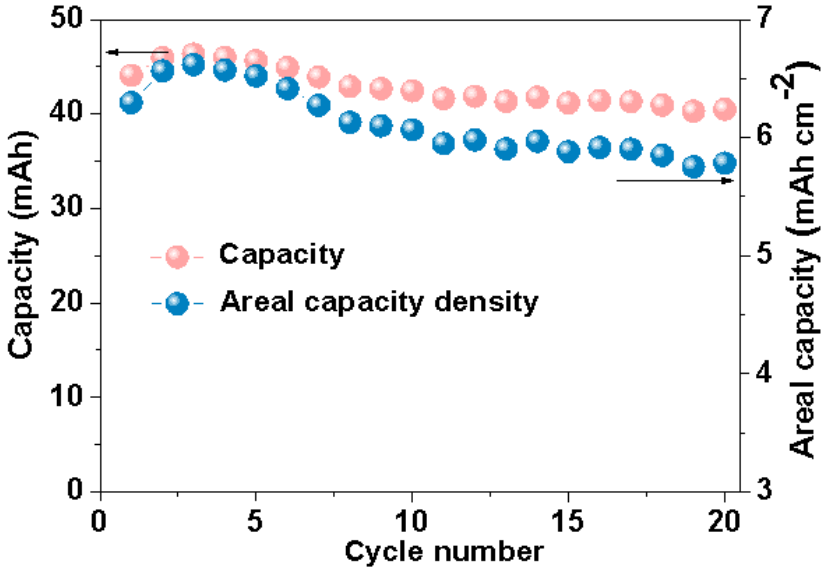

Fig. S22. Total discharge capacity and areal capacity of LCO/Li-Sb-Sn pouch cell (2.5 cm × 2.8 cm). The LCO cathode is 130 μm thick and the initial Li-Sb-Sn is 50 μm thick. The orange is total discharge capacity and the blue is the areal capacity.

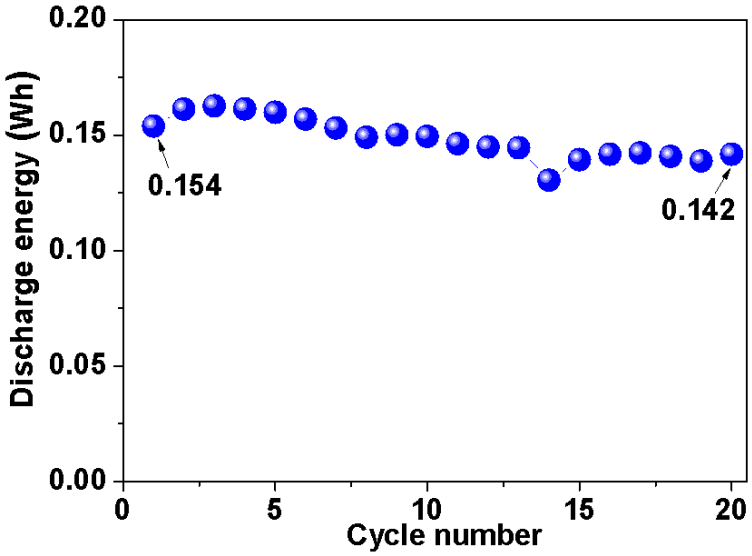

Fig. S23. Discharge energy of LCO/Li-Sb-Sn pouch cell.

Tab. S3. Volumetric energy calculation of LCO/Li-Sb-Sn pouch cell

Cycle number	**1st**	**20th**
Dimension $_{LCO}$ (cm)	2.5 × 2.8 × 0.013	2.5 × 2.8 × 0.013
Dimension $_{Li\text{-}Sb\text{-}Sn}$ (cm)	2.5 × 2.8 × 0.0075	2.5 × 2.8 × 0.0093
Discharge Energy (Wh)	0.154	0.142
Volumetric Energy Density (Wh L^{-1})	1073	909

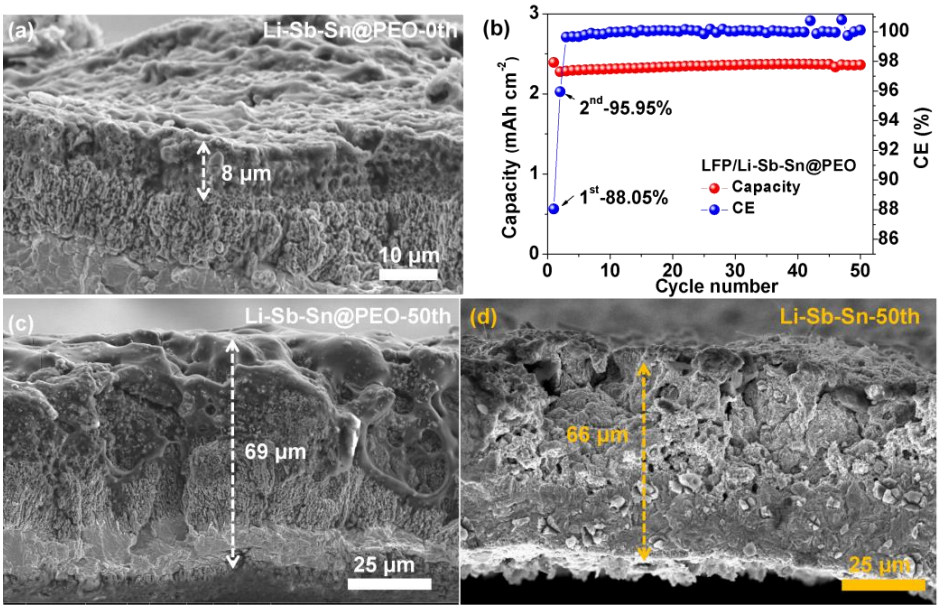

Fig. S24. Full-cell performance of Li-Sb-Sn@PEO protected with an artificial PEO SEI. a) SEM observation of Li-Sb-Sn@PEO observation before full-cell cycling. b) Cycle performance of LFP/Li-Sb-Sn@PEO cell. c) SEM observation of Li-Sb-Sn@PEO electrode after 50 cycles. d) SEM observation of the naked Li-Sb-Sn after 50 cycles.

As stated in this paper, we divided the apparent thickening of alloy electrode into large porosity and excessive SEI. Thus, building an artificial SEI should be very effective to avoid excessive SEI thickening. Inspired by Zhang[5], we roughly coated a layer of PEO on Li-Sb-Sn surface. As shown in Fig. S24a, the artificial SEI is ~8 μm thick so the total thickness of Li-Sb-Sn@PEO is ~58 μm. Although the initial Columbic efficiency (ICE) of Li-Sb-Sn@PEO is slightly lower than the naked Li-Sb-Sn, e.g. Li-Sb-Sn@PEO is 88.5% (Fig. S24b) and Li-Sb-Sn is ~92%, LFP/Li-Sb-Sn@PEO cell can perform stably after activation. The lower ICE may be because the polymer consumes Li^+ for side reactions during first cycles. After 50 cycles, the Li-Sb-Sn@PEO thickened by ~11 μm, e.g. from initial 58 μm to 69 μm (see Fig. S24c), but the naked Li-Sb-Sn thickened by ~16 μm, e.g. from 50 μm to 66 μm (see Fig. S24d). Furthermore, compared to the porous structure of Li-Sb-Sn, the reaction layer of Li-Sb-Sn@PEO showed denser, indicating less electrolyte corrosion after coating PEO.

In future work, we believe the performance of Li-Sb-Sn can be further improved by more carefully designing protective SEI by some exquisite methods, e.g. in-situ reaction to build an artificial host[6], or constructing a robust dual-phase artificial interface by a garnet and a lithiated Nafion layer on the surface of Li-Sb-Sn[7].

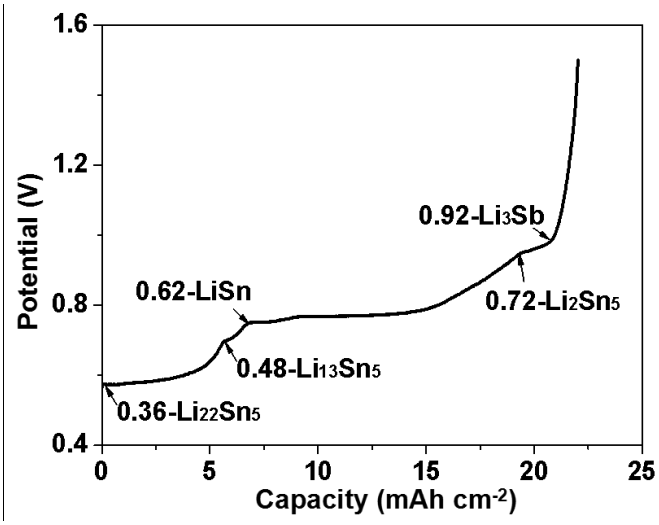

Fig. S25. Lithium inventory of Li-Sb-Sn electrode for fabrication of Li-Sb-Sn/Li-Sb-Sn symmetrical cell. The 200 μm thick Li-Sb-Sn was prepared by rolling one 180 μm Li_{BCC} foil on one 120 μm 5wt%Sb-95wt%Sn foil, with similar amount of area expansion as before (180 μm/1.44 = 125 μm of Li_{BCC} reacting with 120 μm/1.44=83 μm 5wt%Sb-95wt%Sn foil). The lithium inventory is determined by delithiating Li_{BCC} to 1.5 V at a current density of 1 mA cm^{-2}.

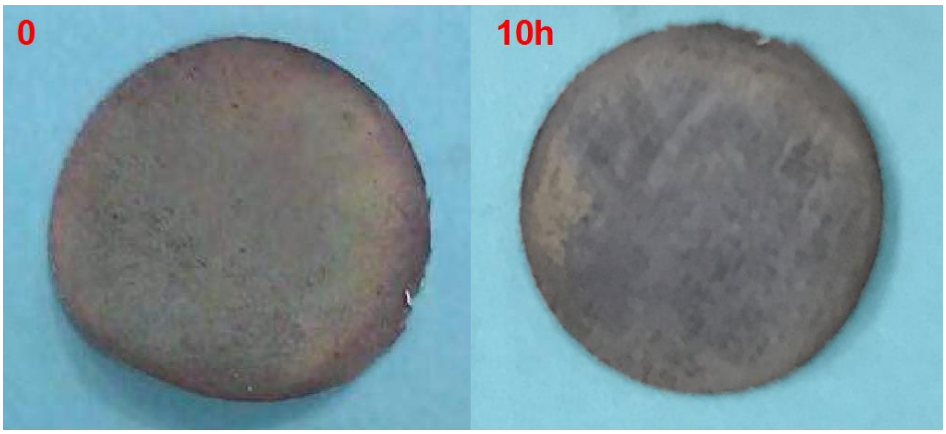

Fig. S26. Digital photos of Li-Sb-Sn electrodes of fresh (the left) and exposed in the air for 10 h (the right). The surface color of Li-Sb-Sn electrode was slightly darkened.

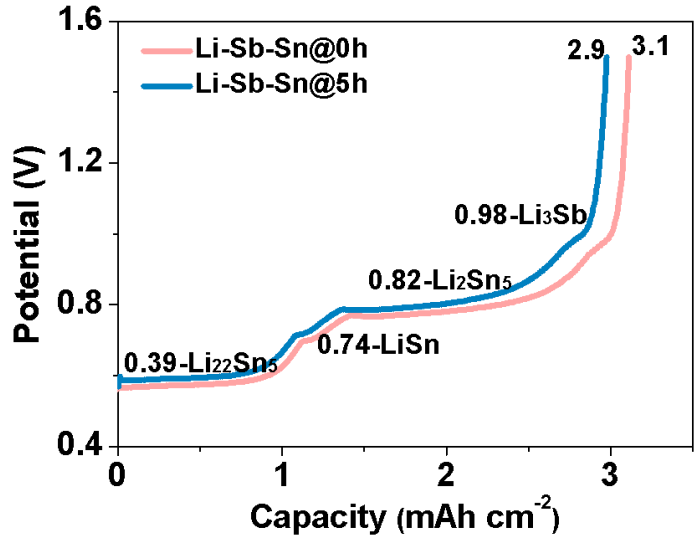

Fig. S27. Delithiation of Li-Sb-Sn electrode of fresh (the orange) and exposed in the air for 10 h (the blue). The capacity retention is up to 93.5% = (2.9/3.1) × 100%.

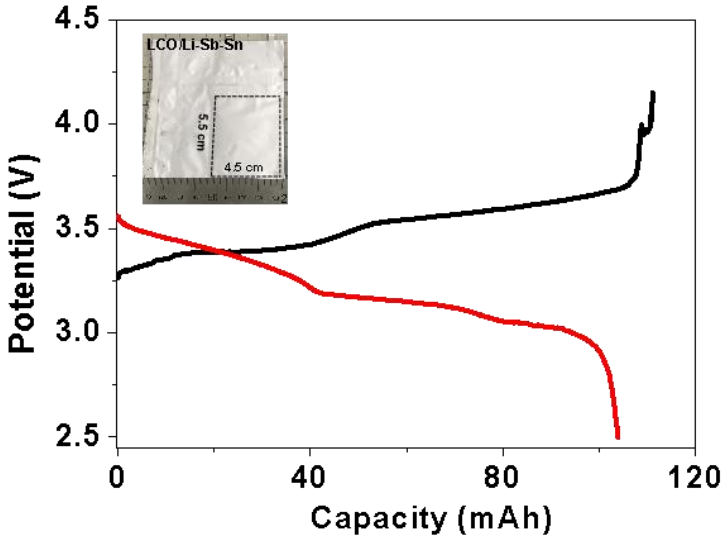

Fig. S28. Potential-Capacity profiles of LCO/Li-Sb-Sn pouch cell for needle piercing experiment. Before measurement, the pouch cell was cycled for 5 cycles. The profiles in the graph are the 1st charge (the black) and discharge curves (the red).

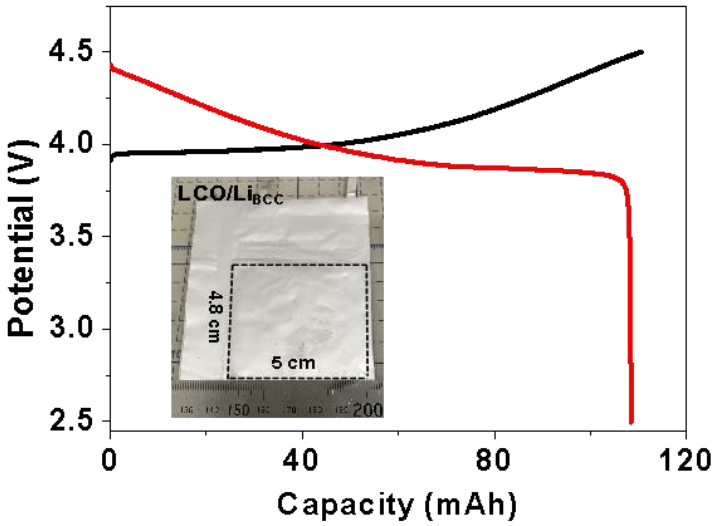

Fig. S29. Potential-Capacity profiles of LCO/Li$_{BCC}$ pouch cell for needle piercing experiment. Before measurement, the pouch cell was cycled for 5 cycles. The profiles in the graph are the 1st charge (the black) and discharge curves (the red).

Supplementary Notes

Calculation details about the proportions of porosity, lithiation product $Li_{22}Sn_5$ and retained soft pure Sn in Li-Sb-Sn and Li-Sn lithiated layer are given as follows:
Firstly, according to the chemical reaction:

$$5\ Sn + 22\ Li \rightarrow Li_{22}Sn_5\ (at\ 0.4\ V)$$

We can calculate the individual thickness of reactant Sn foil, Li foil and product $Li_{22}Sn_5$ based on the following equation:

$$\frac{7.28 \times S_{Sn} \times T_{Sn}}{118.71} : \frac{0.534 \times S_{Li} \times T_{Li}}{6.941} : \frac{2.58 \times S_{Li_{22}Sn_5} \times T_{Li_{22}Sn_5}}{149.25} = 5 : 22 : 1 \quad \text{(S2)}$$

Where 7.28 g cm^{-3}, 0.534 g cm^{-3} and 2.58 g cm^{-3} respectively is the density of Sn, Li and $Li_{22}Sn_5$; 118.71, 6.941 and 149.25 respectively is relative atomic mass of Sn, Li and $Li_{22}Sn_5$; S_{Sn}, S_{Li} individually is reaction area of Sn and Li foils, and $S_{Li22Sn5}$ is the area of lithiation product $Li_{22}Sn_5$. Note that, here, we assume the areas of Sn, Li and $Li_{22}Sn_5$ are identical. T_{Sn}, T_{Li} respectively is the reaction thickness of Sn foil and Li foil, and $T_{Li22Sn5}$ is the thickness of lithiation product $Li_{22}Sn_5$.

Since XRD result of Li-Sb-Sn only determined the presence of $Li_{22}Sn_5$, in order to simplify the calculation process, we assume $Li_{22}Sn_5$ is the only lithiation product. Thus, according to the calculation based on formula (S2), to absorb 25 μm worth of Li_{BCC}, at least 7.13 μm worth of Sn is needed, and forming 25.29 μm worth of $Li_{22}Sn_5$.

Thus, for a Sn based foil of 50 μm thick, there is 42.87 μm = (50-7.13) μm thick Sn foil not involved in reactions, which is clearly still fully dense.

So, after absorbing 25 μm Li_{BCC}, the theoretically total electrode thickness ($t_{theoretically\ total}$) (porous reacted layer + residual dense Sn) should be 68.16 μm = 25.29 μm + 42.87 μm. According to Yu [8], the porosity is calculated by the following formula,

$$p \equiv (E[t_{actually\ total}] - (t_{theoretically\ total}/\alpha)/t_{react} \quad \text{(S3)}$$

Where, p is porosity of reacted layer; $E[t_{actually\ total}]$ is the actually total lithiated electrode thickness obtained by experiment measurements; $t_{theoretically\ total}$ is 68.16 μm; α is coefficient of lateral areal expansion; t_{react} is statistically average reacted thickness.

Supplementary Note 1: Calculation details about proportions of porosity, retained Sn and $Li_{22}Sn_5$ in the reacted layer of Li-Sb-Sn electrode

In order to calculate porosity (p), according to formula (S3), the values of $E[t_{actually\ total}]$, α and t_{react}, need to be determined firstly. Here, we measured the values of $E[t_{actually\ total}]$ and t_{react} by SEM observation of Fig. S30, and the thicknesses of 20 sites were measured for determining $E[t_{actually\ total}]$ and t_{react}.

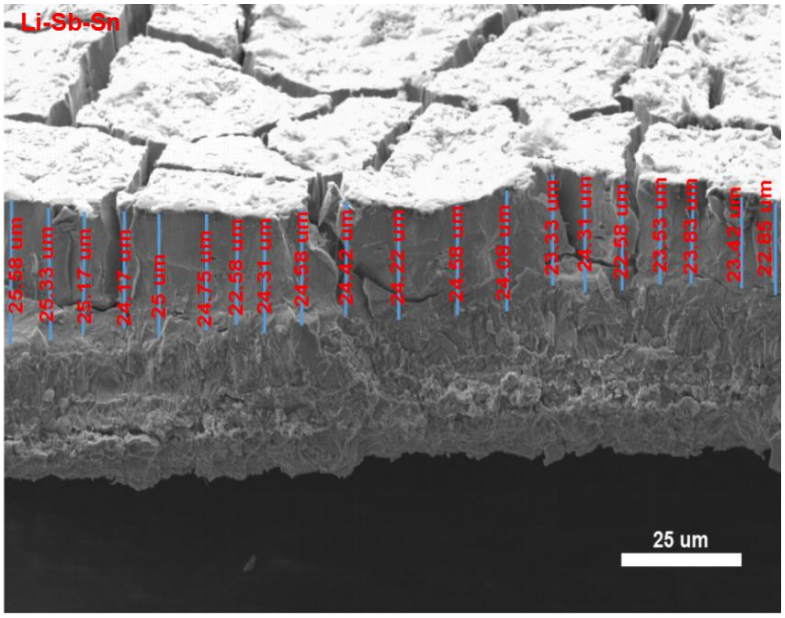

Fig. S30. Measuring reacted layer thickness of Li-Sb-Sn electrode. The measured thicknesses were listed in the following Tab. S4, and its average thickness of reaction layer and standard deviation also were calculated.

Tab. S4. Thickness of reacted layer in Li-Sb-Sn

	Thickness (μm) of reacted layer					Average thickness	Standard Deviation	Reacted layer thickness t_{react}
Li-Sb-Sn	25.58	25.33	25.17	24.17	25	24.13 μm	0.87 μm	24.13±0.87 μm
	24.75	22.58	24.31	24.58	24.42			
	24.22	24.58	24.08	23.33	24.31			
	22.58	23.58	23.83	23.42	22.85			

Thicknesses of the reacted layer and unreacted layer in Li-Sb-Sn were listed in following Tab. S5.

Tab. S5. Thicknesses about reacted layer and unreacted layer of Li-Sb-Sn

Sample	5wt%Sb-95wt%Sn	Li-Sb-Sn
Actually total thickness (μm)	50	50
Reacted layer (t_{react}) (μm)	--	24.13
Unreacted layer ($t_{unreact}$) (μm)	--	25.87

In summary, for the as-prepared Li-Sb-Sn foil electrode, E[$t_{actually\ total}$] is 50 μm, $t_{theoretically\ total}$ is 68.16 μm, α is 1.44 (see Tab. S1) and t_{react} is 24.13 μm.

So, the porosity of reacted layer is

$$11.05\% = (50\ \mu m - 68.16\ \mu m/1.44)/24.13\ \mu m$$

Due to the lateral areal expansion of 144% (see Tab. S1), the lithium foil actually is thinned to

17.36 μm = (50 μm/2) /1.44,

5wt%Sb-95wt%Sn foil is thinned to

34.72 μm = 50 μm/1.44

According to Tab. S5, where 25.87 μm thick 5wt%Sb-95wt%Sn is no involved in reactions, so the actual thickness of Sn involved in lithiation reactions is

8.85 μm = (34.72-25.87) μm

Due to the assumption that $Li_{4.4}Sn$ was the only lithiation product, thus, at least 6.4 μm worth of Sn is needed for absorbing 17.36 μm worth of Li_{BCC}, forming 17.56 μm worth of $Li_{22}Sn_5$. So there is 2.45 μm=8.85 μm-6.4 μm residual pure soft Sn ("retained Sn") in the reacted layer, accounting for

10.15%=2.45 μm/24.13 μm

So, the proportion of $Li_{22}Sn_5$ is

78.8%=100%-11.05%-10.15%

Note that there is some little deviation, e.g. if calculating the proportion of $Li_{22}Sn_5$ based on theoretical thickness of $Li_{22}Sn_5$ (e.g. 17.56 μm) after Sn totally absorbs 17.36 μm Li_{BCC}, the proportion of $Li_{22}Sn_5$ should be

72.77%=17.56 μm /24.13 μm

We speculate such deviation is because the formation of Li_3Sb is not taken into account in this calculation.

Supplementary Note 2: Calculation details of porosity, retained Sn and $Li_{22}Sn_5$ proportions in reacted layer of Li-Sn

Firstly, we determined the lateral areal expansion α of Li-Sn prepared by rolling two 2 cm × 2 cm × 50 μm pure Sn foils sandwiching one 2 cm × 2 cm × 50 μm lithium foil in the middle. After prelithiation, the area expanded to 6.75 cm^2 = 2.7 cm × 2.5 cm (Fig. S31, the right) from the initial 4 cm^2 = 2 cm × 2 cm of Sn foil (Fig. S31, the right). The lateral areal expansion α of Li-Sn is 169% = 6.75 cm^2/4 cm^2. All details were listed in following Tab. S6.

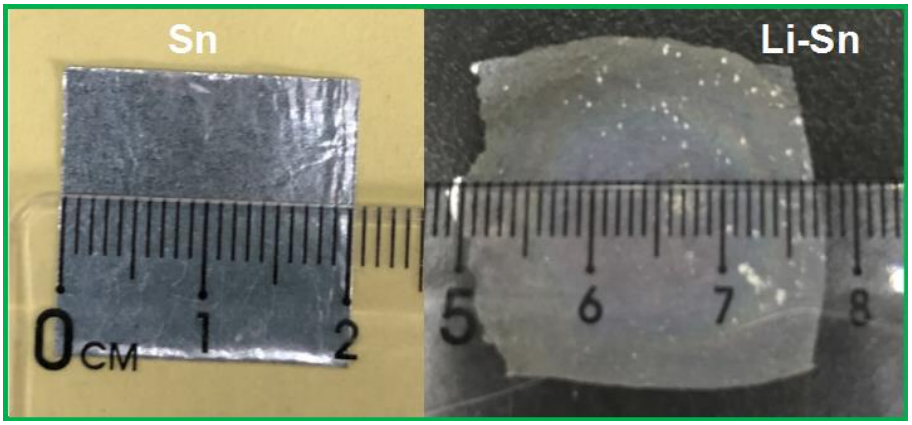

Fig. S31. Dimension size measurement of pure Sn foil before and after MP.

Tab. S6. Dimension size of pure Sn foil before and after MP

Sample	Sn
Size (cm, Before MP)	2×2
Size (cm, After MP)	2.7×2.5
Lateral areal expansion	169%
α	1.69

The reacted layer thickness t_{react} and E[$t_{actually\ total}$] of Li-Sn were measured by SEM image in Fig. S32. The measured thicknesses were listed in the following Tab. S7, the average thickness of reacted layer was also calculated.

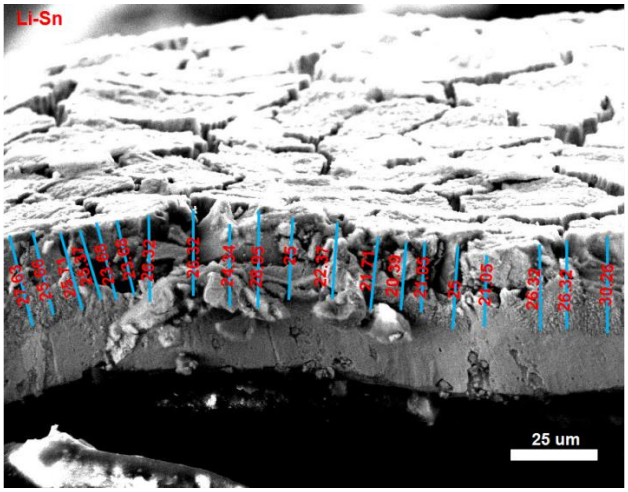

Fig. S32. Thickness measurements of the reaction layer in Li-Sn foil by SEM. The thicknesses of 20 sites in the reacted layer were measured.

Tab. S7. Reacted layer thickness of Li-Sn

	Thickness (μm) of the reacted layer					Average thickness	Standard Deviation	Reacted layer thickness t_{react}
Li-Sn	27.63	25.66	25.71	25.37	23.68	24.86 μm	2.64 μm	24.86±2.64 μm
	23.68	26.32	26.32	24.34	28.95			
	25	22.37	21.71	20.39	21.05			
	25	21.05	26.32	26.32	30.26			

Thicknesses of reacted layer and unreacted layer in Li-Sn electrode were measured and listed in following Tab. S8,

Tab. S8. Thicknesses of reacted layer and unreacted layer in Li-Sn electrode

Sample	Sn	Li-Sn
Actually total thickness (μm)	50	46.05
Reacted layer (t_{react}) (μm)	--	24.86
Unreacted layer ($t_{unreact}$) (μm)	--	21.19

Thus, E[$t_{actually\ total}$] of the as-formed Li-Sn foil electrode is 46.05 μm (Tab. S8), $t_{theoretically\ total}$ is 68.16 μm, α is 1.69 (Tab. S6) and t_{react} is 24.86 μm (see Tab. S8).

The porosity of reacted layer in the as-obtained Li-Sn is

23 % = (46.05 μm -68.16 μm/1.69)/24.86 μm

Due to the lateral areal expansion of 169%, the lithium foil is thinned to

14.79 μm = (50 μm/2) /1.69

Pure Sn foil is thinned to

29.59 μm =50 μm/1.69

According to Tab. S8, there is 21.19 μm thick Sn no involved in reactions, so the actual thickness of Sn involved in lithiation reactions is

8.4 μm = (29.59-21.19) μm

Due to the assumption that $Li_{4.4}Sn$ is the only lithiation product (see Fig. S33), thus, at least 4.22 μm worth of Sn is needed for absorbing 14.79 μm worth of Li_{BCC}, forming 14.96 μm worth of $Li_{22}Sn_5$.

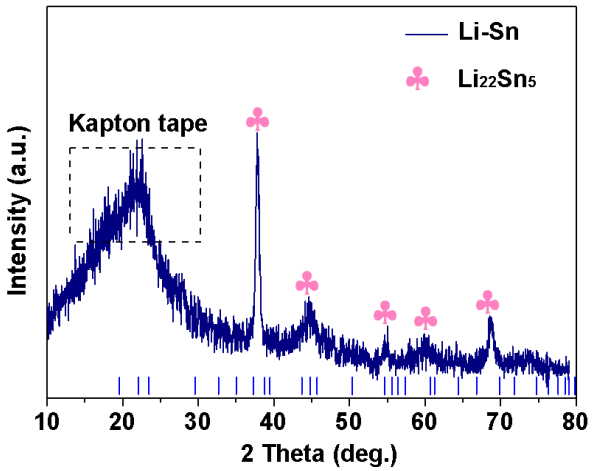

Fig. S33. XRD results of the Li-Sn. According to analysis (PDF#-18-0753), the characteristic peaks belong to $Li_{22}Sn_5$.

So there is 4.18 μm=8.4 μm-4.22 μm thick residual soft Sn ("retained Sn") in the reacted layer, accounting for

16.81%=4.18 μm/24.86 μm

So, the proportion of $Li_{22}Sn_5$ is

60.19%=100%-23%-16.81%

We find the calculation is quite reasonable, evidenced by the calculated percentage of $Li_{22}Sn_5$ 60.18%=14.96 μm /24.86 μm, based on the theoretically formed $Li_{4.4}Sn$ thickness of 14.96 μm after absorbing lithium foil of 14.79 μm by 4.22 μm Sn, which almost is equal to 60.19%.

In order to compare the composition differences between Li-Sb-Sn and Li-Sn more clearly, we also plot the proportion of Li-Sn in the following graph:

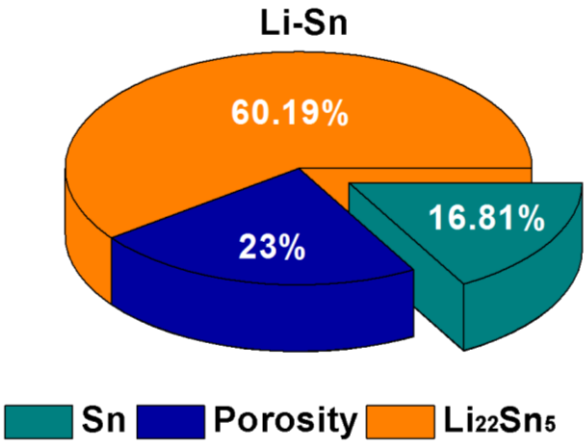

Fig. S34. Proportion of individual composition in Li-Sn foil reacted layer. The olive is residual Sn, the navy is porosity and the orange is $Li_{22}Sn_5$.

Reference

[1] H. Xu, S. Li, X. Chen, C. Zhang, W. Liu, H. Fan, Y. Yu, Y. Huang & J. Li. Sn-Alloy Foil Electrode with Mechanical Prelithiation: Full-Cell Performance up to 200 Cycles. Advanced Energy Materials 0, 1902150, https://doi.org/10.1002/aenm.201902150.

[2] H. Fan, B. Chen, S. Li, Y. Yu, H. Xu, M. Jiang, Y. Huang & J. Li. Nanocrystalline Li–Al–Mn–Si Foil as Reversible Li Host: Electronic Percolation and Electrochemical Cycling Stability. Nano Lett 20, 896-904, https://doi.org/10.1021/acs.nanolett.9b03626 (2020).

[3] H. Xu, S. Li, C. Zhang, X. Chen, W. Liu, Y. Zheng, Y. Xie, Y. Huang & J. Li. Roll-to-roll prelithiation of Sn foil anode suppresses gassing and enables stable full-cell cycling of lithium ion batteries. Energy & Environmental Science 12, 2991-3000, https://doi.org/10.1039/C9EE01404G (2019).

[4] M. Winter & J. O. Besenhard. Electrochemical lithiation of tin and tin-based intermetallics and composites. Electrochim Acta 31, 31-48 (2010), https://doi.org/10.1002/chin.200003257.

[5] R. Xu, X.-B. Cheng, C. Yan, X.-Q. Zhang, Y. Xiao, C.-Z. Zhao, J.-Q. Huang & Q. Zhang. Artificial Interphases for Highly Stable Lithium Metal Anode. Matter 1, 317-344, https://doi.org/10.1016/j.matt.2019.05.016 (2019).

[6] Y. Yuan, F. Wu, G. Chen, Y. Bai & C. Wu. Porous LiF layer fabricated by a facile chemical method toward dendrite-free lithium metal anode. Journal of Energy Chemistry 37, 197-203, https://doi.org/10.1016/j.jechem.2019.03.014 (2019).

[7] R. Xu, Y. Xiao, R. Zhang, X.-B. Cheng, C.-Z. Zhao, X.-Q. Zhang, C. Yan, Q. Zhang & J.-Q. Huang. Dual-Phase Single-Ion Pathway Interfaces for Robust Lithium Metal in Working Batteries. Advanced Materials 31, 1808392, https://doi.org/10.1002/adma.201808392 (2019).

[8] Y. Yu, S. Li, H. Fan, H. Xu, M. Jiang, Y. Huang, J. Li, Optimal annealing of Al foil anode for prelithiation and full-cell cycling in Li-ion battery: The role of grain boundaries in lithiation/delithiation ductility, Nano Energy. 67 (2020) 104274, https://doi.org/10.1016/j.nanoen.2019.104274.

Supplementary Video

Video S1: Burning Li_{BCC} metal with flame

http://li.mit.edu/S/HuiXu/Upload/Burning-Limetal.mp4
Video S2: Burning Li-Sb-Sn electrode with flame
http://li.mit.edu/S/HuiXu/Upload/BurningLi-Sb-Sn.mp4
Video S3: Needle piercing experiment of LCO/Li_{BCC} pouch cell
http://li.mit.edu/S/HuiXu/Upload/Puncturemeasurement-LCO-Lipouch.mp4
Video S4: Needle piercing experiment of LCO/Li-Sb-Sn pouch cell
http://li.mit.edu/S/HuiXu/Upload/Puncturemeasurement-LCO-Li-Sb-Snpouch.mp4